Compositional evolution of the upper continental crust through time, as constrained by ancient glacial diamictites

Richard M. Gaschnig [a,*], Roberta L. Rudnick [a,1], William F. McDonough [a],
Alan J. Kaufman [b], John W. Valley [c], Zhaochu Hu [d], Shan Gao [d,2], Michelle L. Beck [e]

[a] Department of Geology, University of Maryland, College Park, MD 20742, United States
[b] Department of Geology and Earth System Science Interdisciplinary Center, University of Maryland, College Park, MD 20742, United States
[c] Department of Geoscience, University of Wisconsin – Madison, Madison, WI 53706, United States
[d] State Key Laboratory of Geological Processes and Mineral Resources, China University of Geosciences, Wuhan 430074, China
[e] Department of Biological Sciences, Virginia Polytechnic Institute and State University, Blacksburg, VA 24061, United States

Abstract

The composition of the fine-grained matrix of glacial diamictites from the Mesoarchean, Paleoproterozoic, Neoproterozoic, and Paleozoic, collected from four modern continents, reflects the secular evolution of the average composition of the upper continental crust (UCC). The effects of localized provenance are present in some cases, but distinctive geochemical signatures exist in diamictites of the same age from different localities, suggesting that these are global signatures. Archean UCC, dominated by greenstone basalts and to a lesser extent komatiites, was more mafic, based on major elements and transition metal trace elements. Temporal changes in oxygen isotope ratios, rare earth elements, and high field strength elements indicate that the UCC became more differentiated and that tonalite–trondhjemite–granodiorite suites became less important with time, findings consistent with previous studies. We also document the concentrations of siderophile and chalcophile elements (Ga, Ge, Cd, In, Sn, Sb, W, Tl, Bi) and lithophile Be in the UCC through time, and use the data for the younger diamictites to construct a new estimate of average UCC along with associated uncertainties.
© 2016 Elsevier Ltd. All rights reserved.

1. INTRODUCTION

The Earth is unique among other terrestrial planets in our solar system in that it has continents, which are composed of silicic crust distinct from the basalts that dominate Earth's ocean basins and the crusts of other planets. Continental crust reflects differentiation associated with plate tectonics on Earth (Taylor and McLennan, 1985; Rudnick, 1995; Condie and Kroner, 2013). How continents form and how they have grown through Earth's history remain salient first-order questions in Earth science (Committee on Grand Research Questions in the Solid-Earth Sciences, National Research Council, 2008). A necessary starting point to deciphering how continents form is knowledge of their bulk composition. The continental crust, especially the upper crust, is enriched in incompatible elements, by as much as a thousand fold relative to the mantle, and thus it exerts a large influence on the planetary budget of these elements, despite comprising a minute proportion (0.5%) of the mass of the silicate Earth. These elements include the heat producing elements (K, Th, and U) that partially power mantle convection and drive plate tectonics. Thus, quantifying the composition of the upper continental crust,

---

* Corresponding author at: School of Earth and Atmospheric Sciences, Georgia Institute of Technology, Atlanta, GA 30332, United States.
[1] Now at Department of Earth Science, University of California – Santa Barbara, Santa Barbara, CA 93106, United States.
[2] Deceased.

the associated uncertainties on that composition, and how this composition may have changed through time is an essential step in constraining the Earth's evolving power budget and, from that, mantle dynamics.

Previous attempts to quantify the average composition of the upper continental crust (UCC) have generally followed one of two approaches: systematic grid-based bedrock sampling, or analysis of fine-grained sediments (or sedimentary rocks) such as shales and loess. The former approach typically involves the collection and analysis of thousands of samples and has been carried out in the Canadian Shield (Shaw et al., 1967, 1976; Eade and Fahrig, 1973), Russia (Ronov and Yaroshevsky, 1967, 1976; Borodin, 1998), China (Gao et al., 1998), and Japan (Togashi et al., 2000). The latter approach assumes that natural geological (sedimentary) processes provide a robust average of insoluble elements in the provenance of the sediments, and has been used in many studies aimed at tracking the compositional evolution of the UCC (Nance and Taylor, 1976, 1977; McLennan et al., 1979,1980, 1983; Taylor and McLennan, 1985, 1995; Wronkiewicz and Condie, 1987, 1989, 1990; Peucker-Ehrenbrink and Jahn, 2001; Kamber et al., 2005; Chauvel et al., 2014; Sauzéat et al., 2015). Most of these studies use either shale, glacially-derived loess, or desert loess to infer the average composition of the UCC, which works well for insoluble elements, but not for soluble elements. Although the cold temperatures and largely physical weathering that produce the glacial loess limits loss of the soluble elements compared with shales, such loess still records a weathering signature (Gallet et al., 1998), and both types of loess are also affected by wind-driven particle sorting that fractionates heavy minerals, which may dominate the budgets of certain elements (e.g., Ti, Zr, Hf, Sn) (Taylor et al., 1983; Liu et al., 1993; Barth et al., 2000; McLennan, 2001; Chauvel et al., 2014; Sauzéat et al., 2015).

By contrast, use of till or its lithified equivalent, glacial diamictite, may avoid many of the above problems. Like loess, till is produced by physical weathering and thus, may be expected to provide useful information on the soluble element concentrations of the UCC. Unlike loess, there is minimal sorting, as tills are not reworked by wind (or water). Goldschmidt (1933, 1958) first suggested the utility of related glacial loam as a proxy for the average composition of the UCC and the use of till for this purpose was recently explored by Canil and Lacourse (2011) in a study of Quaternary valley till in the Canadian Cordillera, who showed that the tills provided robust averages of the bedrock in the valleys the glaciers sampled.

Here, we report the major, trace element and oxygen isotopic compositions of pre-Cenozoic diamictites deposited by continental ice sheets, and use these diamictites to evaluate the compositional evolution of the UCC, for both soluble and insoluble elements, as well as elements for which few data existed previously (e.g., Be, Ga, Ge, Cd, In, Sn, Sb, W, Tl, Bi). The diamictites studied here were identified by previous workers as being of glacial origin based on the presence of faceted and striated clasts, the presence of dropstones in associated laminated sediments, as well as aspects of stratigraphic facies architecture (e.g., Hambrey and Harland, 1981). We hereafter refer to these rocks as diamictites, with the understanding that all samples investigated here have been proposed to be of glacial origin.

2. METHODS

2.1. Samples and their preparation

Glacial diamictites deposited by continental ice sheets are recognized around the world from four pre-Cenozoic intervals (~2.9, 2.4–2.2, 0.75–0.57, and 0.30 Ga); we sampled diamictites from all four intervals on several modern continents. Stratigraphic units, ages, localities, and references to the original investigations of these units are given in Table 1.

The samples investigated here comprise two rock types: (1) most samples comprise massive (i.e., un-stratified) diamictite, which consists of muddy to sandy matrix material with clasts ranging from pebble to cobble size, and (2) a few samples are dropstone-bearing argillites, which are fine-grained stratified sedimentary rocks spatially associated with the diamictites. In both cases, our analytical campaign focused on the fine-grained matrix material. Pieces with fewer clasts were selected from each sample and crushed to chips in an alumina jaw crusher. Any chips containing clasts larger than ~5 mm were then removed by hand. A fraction of the remaining material was then ground to a fine powder in an alumina swing mill. We endeavored to produce 100 g of powder for each sample, although this was not possible with some clast-rich varieties.

In addition to preparing individual samples for analysis, we also prepared composite samples of each stratigraphic unit, with the exceptions of the Paleoproterozoic Pecors, Neoproterozoic Blasskranz, and Ordovician Pakhuis formations, for which we have no more than two samples each. Each composite sample consists of equal weights of powder from each individual sample of a stratigraphic unit that were thoroughly mixed together. These composites are intended to serve as a new upper crustal reference suite of samples, comparable to PAAS (post-Archean Australian shale; Nance and Taylor, 1976) and NASC (North American shale composite; Haskin et al., 1966), and represent average compositions of the glacially sampled upper crust found in each stratigraphic unit. The composites are available for further investigations upon request to the second author.

2.2. X-ray fluorescence analysis

Major element concentrations and a limited number of trace elements were determined by XRF at Franklin and Marshall College. Loss of ignition (LOI) was first determined at 900 °C. From the resulting anhydrous powder, 0.4 g were mixed with 3.6 g of lithium tetraborate flux and fused in a platinum crucible. The fusion disc was used for measurement of major elements, along with Sr, Zr, V, and Cr. Other trace elements were measured on a powder briquette made with copolywax binder. Analyses were conducted on a PANalytical 2404 X-ray XRF vacuum spectrometer with a 4 kW super sharp X-ray tube. Major element results for the composite samples are new and

Table 1
Glacial diamictites investigated in this study.

Stratigraphic unit	Country (state/province)	Drill core or outcrop?	General references	Approximate age (Ga)
Archean				
Mozaan Grp	S Africa	O	Young et al. (1998)	2.9
Afrikander Frm[*]	S Africa	O	Guy et al. (2010)	2.9
Coronation Frm[*]	S Africa	DC	Guy et al. (2010)	2.9
Promise Frm[*]	S Africa	DC	Guy et al. (2010)	2.9
Paleoproterozoic				
Duitschland Frm	S Africa	DC	Melezhik et al. (2013)	2.4
Timeball Hill Frm[**]	S Africa	DC	Melezhik et al. (2013)	2.2
Makganyene Frm	S Africa	DC	Melezhik et al. (2013)	2.3
Ramsay Lake Frm	Canada (Ontario)	O	Melezhik et al. (2013)	2.4
Pecors Frm	Canada (Ontario)	O	Melezhik et al. (2013)	2.4
Bruce Frm	Canada (Ontario)	O	Melezhik et al. (2013)	2.4
Gowganda Frm	Canada (Ontario)	O	Melezhik et al. (2013)	2.4
Bottle Creek Frm	USA (Wyoming)	O	Houston et al. (1992)	2.4
Neoproterozoic				
Pocatello Frm	USA (Idaho)	O	Keeley et al. (2013)	0.7
Konnarock Frm	USA (Virginia)	O	Rankin (1993)	0.7
Gaskiers Frm	Canada (Newfoundland)	O	Carto and Eyles (2011)	0.58
Nantuo Frm	China (Hubei)	O	Zhou et al. (2004)	0.64
Gucheng Frm	China (Hubei)	O	Liu et al. (2008)	0.7
Blaubeker Frm	Namibia	O	Prave et al. (2011)	0.7
Kaigas Frm	Namibia	O	Frimmel (2011)	0.75
Blasskranz	Namibia	O	Kaufman et al. (2010)	0.64
Chuos Frm	Namibia	O	Le Heron et al. (2013)	0.7
Numees Frm	Namibia	O	Frimmel (2011)	0.6
Ghaub Frm	Namibia	O	Hoffman (2011)	0.64
Paleozoic				
Machareti Group	Bolivia	O	Starck and Papa (2006)	0.3
Mandiyuti Group	Bolivia	O	Starck and Papa (2006)	0.3
Pakhuis Frm	S Africa	DC	Young et al. (2004)	0.44
Dwyka Group	S Africa and Namibia	O & DC	Visser (1982)	0.3

O = outcrop, DC = drill core.

[*] The Afrikander, Coronation, and Promise Formations are components of the Witwatersrand Supergroup and are grouped as such in figures. Note that the Afrikander diamictite is sometimes referred to as the Lagerspoort or the Blue Grit diamictite in the literature.

[**] The Timeball Hill diamictite is sometimes referred to as the Rietfontein diamictite in the literature.

reported in Table 2, whereas results for the individual samples were previously reported in Gaschnig et al. (2014) and are provided here for completeness in Supplemental Table B.1. Trace elements by XRF are reported and discussed in the Supplemental material.

2.3. ICP-MS analysis

2.3.1. Sample digestion

Most samples were digested by conventional high pressure HF/HNO$_3$ dissolution in Teflon Parr bombs, closely following the methods of Zhang et al. (2012b). For each sample, fifty milligrams of powder was weighed into a bomb along with 1 mL and 3 mL of concentrated HNO$_3$ and HF, respectively. Bombs were then capped and placed in an oven for at least 4 days at ~180 °C. Bombs were then opened and acids were evaporated on a hot plate. Two mL of concentrated HNO$_3$ were added to the salt and evaporated, followed by 1 mL of HNO$_3$ with 2 mL of H$_2$O. Bombs were then capped and returned to the oven for one day at 150 °C. Samples were transferred to centrifuge

capsules and diluted to 15 mL using 2% HNO$_3$ containing a trace of HF.

A subset of samples (Paleoproterozoic samples from Wyoming and Ontario and Paleozoic samples from Bolivia) was digested using the NH$_4$HF$_2$ method developed by Zhang et al. (2012a). In this method, ~0.2 g of purified NH$_4$HF$_2$ was added to 0.05 g of sample powder with a drop of water in a Teflon screw-top Savillex beaker. Beakers were placed in an oven for 12 h at ~230 °C. Upon returning to room temperature, 2 mL of HNO$_3$ were added to the solid salt and the beakers were capped and placed on the hot plate at 160 °C for at least an hour. Beakers were then uncapped and solutions were evaporated. One mL of HNO$_3$ and 2 mL of H$_2$O were added to the salt and the beaker was capped and placed on the hot plate for at least 6 h. Samples were transferred to centrifuge capsules and diluted to 15 mL with 2% HNO$_3$ containing a trace of HF.

Due to the large range in concentration of the elements analyzed (spanning five orders of magnitude, with Fe and Bi as end members) two dilutions were prepared for analysis from the master sample aliquot. The first dilution was

Table 2
Major and trace element data for composite samples.

Sample	Age	SiO₂ XRF[*]	TiO₂	Al₂O₃	Fe₂O₃(T)	MnO	MgO	CaO	Na₂O	K₂O	P₂O₅	**LOI**[**]	**CIA**[***]	M%[****]	W%[****]	F%[****]	Li ICPMS	Be	Sc	V
Composites																				
Mozaan	Mesoarchean	57.2	0.37	8.70	25.0	0.13	3.00	0.44	0.55	1.40	0.06	3.07	74	20	75	5	24.3	1.00	10.7	78.3
Afrkiander	Mesoarchean	63.3	0.24	8.45	8.40	0.14	9.31	6.04	0.56	0.59	0.04	2.95	77	37	56	7	23.2	0.367	20.1	113
Coronation	Mesoarchean	72.0	0.49	14.8	4.04	0.05	1.92	0.36	0.32	2.87	0.07	3.05	78	7	84	9	41.3	1.40	11.4	79.7
Promise	Mesoarchean	70.3	0.38	11.0	9.51	0.08	2.65	0.80	0.64	1.47	0.04	3.10	75	22	66	11	55.8	0.777	7.93	68.3
Ramsay Lake	Paleoproterozoic	67.9	0.55	12.7	7.73	0.10	3.23	1.02	1.44	2.08	0.14	3.12	67	31	50	19	62.0	1.32	11.5	102
Gowganda	Paleoproterozoic	65.8	0.54	14.7	6.36	0.07	2.60	0.93	4.64	2.00	0.14	2.18	57	31	32	36	22.6	1.98	13.7	112
Bottle Creek	Paleoproterozoic	71.0	0.45	13.3	4.19	0.05	2.50	0.52	4.15	1.91	0.12	1.77	58	21	39	40	13.3	1.65	9.59	81.5
Bruce	Paleoproterozoic	67.9	0.46	14.8	4.55	0.02	3.20	0.35	3.72	2.71	0.10	2.25	61	15	50	35	28.8	3.06	11.3	105
Makganyene	Paleoproterozoic	56.7	0.38	8.30	18.4	0.39	3.96	3.36	0.06	1.01	0.09	7.31	89	0	100	0	21.7	1.52	8.27	57.2
Timeball	Paleoproterozoic	65.0	0.55	15.5	7.52	0.07	1.61	1.58	1.37	3.19	0.15	3.46	66	25	47	28	31.6	2.64	11.3	101
Duitschland	Paleoproterozoic	55.1	0.70	14.7	12.0	0.29	2.73	2.87	0.08	3.00	0.14	8.41	82	0	99	0	59.1	1.90	15.8	143
Konnarock	Neoproterozoic	67.5	0.74	14.0	5.24	0.08	1.50	1.20	2.69	4.44	0.21	2.40	56	22	37	41	25.7	3.70	11.5	69.9
Gaskiers	Neoproterozoic	66.8	0.68	14.9	5.18	0.11	1.66	1.15	3.57	3.27	0.14	2.58	57	25	32	43	37.3	2.35	14.2	77.9
Pocatello	Neoproterozoic	69.3	1.10	12.7	6.34	0.08	1.68	0.74	1.05	3.84	0.26	2.91	66	14	71	15	30.7	4.20	10.5	85.4
Nantuo	Neoproterozoic	65.1	0.61	14.3	5.64	0.13	2.40	1.82	1.26	3.30	0.12	5.28	65	26	48	26	38.3	2.16	10.8	74.7
Gucheng	Neoproterozoic	66.5	0.62	14.3	5.36	0.66	2.05	1.10	1.03	3.37	0.14	4.89	67	22	54	24	38.7	2.34	13.5	72.5
Blaubeker	Neoproterozoic	76.8	0.49	9.87	3.90	0.05	1.35	0.55	1.67	3.07	0.12	2.08	59	14	50	35	25.3	1.51	7.42	66.5
Kaigas	Neoproterozoic	63.8	0.78	15.1	6.07	0.10	2.38	2.20	2.62	3.33	0.19	3.37	57	38	29	33	40.4	3.41	15.4	98.2
Chuos	Neoproterozoic	47.1	0.45	8.28	7.41	0.75	6.45	10.72	1.13	2.39	0.22	15.13	58	42	42	15	41.4	1.86	9.27	63.9
Numees	Neoproterozoic	70.7	0.47	12.6	3.71	0.07	1.51	1.93	1.97	3.91	0.16	2.96	54	24	27	49	25.9	2.89	8.69	57.2
Ghaub	Neoproterozoic	32.0	0.35	7.23	3.35	0.05	3.00	26.86	0.60	2.18	0.14	24.23	64	27	55	18	26.6	1.18	7.81	78.4
Bolivia	Paleozoic	73.6	0.62	12.3	3.87	0.05	1.58	0.40	1.10	2.80	0.12	3.56	70	10	70	20	45.3	2.40	9.74	63.8
Dwyka East	Paleozoic	67.3	0.64	13.9	5.41	0.09	2.29	1.57	3.16	2.96	0.18	2.58	56	32	29	38	30.8	2.38	10.8	81.5
Dwyka West	Paleozoic	42.8	0.44	8.76	9.77	0.70	8.01	10.40	0.90	1.72	0.13	16.36	65	44	47	9	31.7	1.14	12.3	124

Sample	Age	Cr	Mn	Co	Ni	Cu	Zn[°°] XRF	Ga[°] ICPMS	Ge	Rb	Sr	Y	Zr	Nb	**Mo**	**Cd**	**In**	**Sn**	**Sb**	Cs	Ba
Composites																					
Mozaan	Mesoarchean	344	902	21.0	141	38.7	57	**11.5**	**3.26**	43.2	68.6	11.5	85.4	5.24	**0.884**	**0.07**	**0.032**	**0.945**	**0.824**	1.99	317
Afrkiander	Mesoarchean	1132	884	41.7	227	41.3	57	**7.85**	**1.49**	13.8	140	9.92	90.1	1.94	**0.471**	**0.068**	**0.027**	**0.385**	**0.599**	0.381	226
Coronation	Mesoarchean	294	253	20.2	114	224	141	**16.9**	**1.09**	99.2	69.1	15.5	220	8.79	**2.97**	**0.770**	**0.086**	**1.58**	**1.67**	8.08	578
Promise	Mesoarchean	386	491	22.2	152	43.5	87	**13.0**	**1.68**	61.9	44.0	10.8	175	5.43	**0.774**	**0.193**	**0.027**	**0.886**	**0.319**	3.24	286
Ramsay Lake	Paleoproterozoic	74.7	598	16.6	39.7	21.8	143	**18.5**	**1.34**	88.2	78.6	17.5	166	7.35	**2.29**	**0.282**	**0.0430**	**1.36**	**0.227**	4.17	368
Gowganda	Paleoproterozoic	121	401	18.9	55.9	19.6	38	**17.7**	**1.02**	67.0	130	15.1	133	7.01	**1.78**	**0.045**	**0.031**	**1.33**	**0.806**	1.24	408
Bottle Creek	Paleoproterozoic	96.2	313	12.5	37.8	48.0	34	**15.0**	**0.950**	62.9	142	10.4	163	5.32	**0.578**	**0.080**	**0.024**	**1.05**	**0.342**	1.84	492
Bruce	Paleoproterozoic	111	116	9.34	32.4	3.06	4	**23.1**	**1.12**	114	84.1	15.8	184	7.71	**1.46**	**0.038**	**0.048**	**1.72**	**0.320**	1.60	428
Makganyene	Paleoproterozoic	82.4	2803	12.8	37.3	30.8	70	**10.3**	**3.78**	30.2	42.2	16.7	89.2	8.46	**1.04**	**0.088**	**0.048**	**2.08**	**1.98**	2.01	162
Timeball	Paleoproterozoic	123	479	14.9	38.7	23.3	79	**18.5**	**1.44**	165	104	20.0	154	9.80	**1.30**	**0.075**	**0.049**	**2.67**	**1.12**	13.0	326
Duitschland	Paleoproterozoic	164	1875	19.4	61.3	7.96	28	**21.2**	**1.80**	124	42.1	30.9	199	14.8	**0.547**	**0.056**	**0.058**	**3.56**	**0.971**	9.30	240
Konnarock	Neoproterozoic	44.7	542	11.3	21.9	11.2	82	**19.4**	**1.35**	170	116	44.2	346	23.4	**0.478**	**0.107**	**0.062**	**2.63**	**0.222**	4.14	795

Sample	Age																				
Gaskiers	Neoproterozoic	25.6	727	9.89	11.4	16.3	79	**16.7**	**1.75**	86.7	187	35.9	185	11.0	**0.559**	**0.078**	**0.068**	**1.87**	**0.642**	5.71	689
Pocatello	Neoproterozoic	64.2	523	14.4	25.9	15.0	107	**17.5**	**1.42**	137	92.1	46.1	422	109	**1.17**	**0.152**	**0.039**	**3.03**	**1.38**	4.26	662
Nantuo	Neoproterozoic	55.7	892	12.2	28.8	27.4	86	**18.9**	**1.92**	101	73.1	28.6	221	11.6	**0.317**	**0.108**	**0.065**	**2.49**	**0.476**	4.84	1080
Gucheng	Neoproterozoic	66.0	4796	13.3	34.9	19.3	96	**17.3**	**1.79**	96.7	44.3	33.6	175	12.1	**0.332**	**0.099**	**0.063**	**2.24**	**0.467**	4.03	924
Blaubeker	Neoproterozoic	39.0	287	4.92	14.1	22.7	42	**11.6**	**1.37**	104	66.8	25.4	248	9.59	**0.490**	**0.091**	**0.045**	**1.89**	**0.594**	2.51	866
Kaigas	Neoproterozoic	58.9	682	15.2	29.5	31.2	96	**20.6**	**1.71**	203	160	33.9	191	22.0	**1.01**	**0.195**	**0.092**	**3.93**	**0.060**	11.3	593
Chuos	Neoproterozoic	31.0	5872	19.1	29.5	24.7	59	**11.2**	**1.35**	92.8	157	23.0	136	17.4	**0.614**	**0.181**	**0.050**	**1.60**	**0.240**	4.83	508
Numees	Neoproterozoic	29.0	438	8.91	16.0	15.6	61	**15.1**	**1.44**	186	126	26.5	249	12.9	**0.425**	**0.132**	**0.058**	**2.38**	**0.191**	5.23	611
Ghaub	Neoproterozoic	44.9	366	6.52	17.4	14.0	44	**9.67**	**1.13**	78.0	523	16.0	114	6.82	**0.463**	**0.128**	**0.039**	**1.54**	**0.438**	8.98	365
Bolivia	Paleozoic	50.0	268	9.87	18.4	6.97	76	**15.2**	**1.50**	110	103	29.0	274	13.3	**0.239**	**0.072**	**0.045**	**2.68**	**0.581**	5.95	400
Dwyka East	Paleozoic	95.4	579	12.8	32.5	19.3	85	**17.8**	**1.30**	107	173	31.5	287	12.5	**0.730**	**0.184**	**0.055**	**2.31**	**0.270**	2.79	773
Dwyka West	Paleozoic	164	5328	25.0	79.9	48.1	106	**11.5**	**1.14**	64.6	85.3	16.7	87.9	7.28	**2.88**	**0.227**	**0.042**	**1.38**	**0.908**	3.41	254

Sample	Age	La	Ce	Pr	Nd	Sm	Eu	Gd	Tb	Dy	Ho	Er	Tm	Yb	Lu	Hf	Ta	W	Tl	Pb	Bi	Th	U	$\delta^{18}O$
Composites																								
Mozaan	Mesoarchean	14.9	29.2	3.47	12.4	2.46	0.597	2.02	0.353	1.97	0.410	1.21	0.175	1.14	0.171	2.26	0.444	**0.71**	0.214	7.32	**0.158**	3.86	1.11	
Afrkiander	Mesoarchean	7.71	15.4	1.79	6.77	1.44	0.426	1.45	0.270	1.70	0.376	1.14	0.174	1.11	0.176	2.12	0.180	**0.28**	0.127	3.97	**0.034**	1.72	0.557	
Coronation	Mesoarchean	29.4	59.9	6.86	24.6	4.49	1.08	3.40	0.525	2.87	0.576	1.70	0.256	1.68	0.260	6.46	0.933	**0.74**	0.704	57.3	**0.275**	9.14	4.88	
Promise	Mesoarchean	17.7	35.7	4.03	14.7	2.79	0.972	2.29	0.376	2.11	0.421	1.25	0.184	1.21	0.185	3.72	0.493	**0.77**	0.470	3.06	**0.183**	4.32	1.42	
Ramsay Lake	Paleoproterozoic	30.6	59.3	6.86	24.6	4.48	0.941	3.49	0.573	3.06	0.615	1.81	0.264	1.73	0.262	3.98	0.701	**2.1**	0.843	36.8	**0.430**	16.2	6.41	
Gowganda	Paleoproterozoic	31.1	60.2	7.03	25.3	4.55	1.04	3.23	0.488	2.64	0.536	1.54	0.223	1.45	0.220	3.67	0.691	**1.6**	0.326	7.92	**0.273**	12.1	3.83	
Bottle Creek	Paleoproterozoic	13.9	27.8	3.54	13.2	2.56	0.643	1.93	0.317	1.81	0.380	1.16	0.175	1.18	0.182	4.44	0.526	**0.81**	0.310	7.98	**0.232**	7.73	2.04	
Bruce	Paleoproterozoic	26.9	51.0	5.93	21.5	4.16	1.02	3.26	0.518	2.88	0.575	1.73	0.266	1.75	0.274	5.39	0.874	**1.4**	0.335	6.66	**0.161**	7.19		
Makganyene	Paleoproterozoic	25.0	48.0	5.42	19.3	3.58	0.709	2.91	0.480	2.67	0.559	1.63	0.240	1.54	0.236	2.65	0.753	**2.0**	0.234	19.9	**0.284**	11.7	3.27	
Timeball	Paleoproterozoic	41.5	79.2	9.05	31.6	5.70	1.29	4.33	0.684	3.62	0.719	2.06	0.301	1.91	0.293	4.41	0.945	**2.2**	0.987	26.4	**0.308**	15.7	4.29	
Duitschland	Paleoproterozoic	51.8	101	11.36	40.0	7.26	1.45	5.74	0.969	5.50	1.16	3.40	0.509	3.15	0.482	5.49	1.49	**4.5**	1.35	26.1	**1.91**	22.1	3.46	
Konnarock	Neoproterozoic	61.5	121	15.49	56.8	10.82	1.93	8.65	1.40	7.59	1.56	4.57	0.658	4.17	0.629	9.22	1.54	**1.1**	0.863	19.6	**0.103**	18.7	3.23	
Gaskiers	Neoproterozoic	27.6	57.6	7.87	31.9	6.77	1.58	6.08	1.05	6.07	1.26	3.74	0.546	3.58	0.552	5.23	0.749	**1.0**	0.431	8.60	**0.188**	8.53	2.21	
Pocatello	Neoproterozoic	92.1	172	20.9	74.3	13.12	2.64	10.5	1.69	8.95	1.71	4.84	0.666	4.11	0.601	11.1	6.80	**2.0**	0.538	13.4	**0.136**	22.8	4.42	
Nantuo	Neoproterozoic	32.4	66.4	7.94	29.7	6.16	1.29	5.23	0.915	5.28	1.11	3.25	0.499	3.18	0.491	5.33	0.891	**1.3**	0.396	16.4	**0.336**	12.7	1.74	
Gucheng	Neoproterozoic	35.4	70.0	8.91	33.7	6.96	1.47	6.14	1.05	6.10	1.23	3.63	0.526	3.34	0.511	5.44	0.944	**1.4**	0.338	12.0	**0.237**	12.6	1.54	
Blaubeker	Neoproterozoic	28.0	55.0	6.65	24.3	4.91	1.02	4.27	0.754	4.32	0.905	2.67	0.393	2.58	0.389	6.36	0.792	**1.1**	0.643	17.1	**0.231**	9.11	2.15	
Kaigas	Neoproterozoic	52.3	100	13.02	47.0	9.27	1.49	7.21	1.18	6.41	1.26	3.59	0.528	3.39	0.503	5.82	2.08	**2.0**	1.17	26.5	**0.692**	26.8	5.62	
Chuos	Neoproterozoic	29.0	57.8	6.93	25.3	4.88	0.989	4.07	0.690	3.91	0.814	2.37	0.350	2.25	0.342	3.67	1.10	**0.78**	0.566	12.6	**0.154**	9.66	1.68	
Numees	Neoproterozoic	38.3	80.0	9.29	33.4	6.40	1.09	5.08	0.869	4.82	0.977	2.86	0.429	2.73	0.409	5.26	0.995	**1.5**	0.864	11.1	**0.495**	18.2	2.74	
Ghaub	Neoproterozoic	15.6	31.6	4.23	16.7	3.44	0.705	2.97	0.515	2.92	0.611	1.79	0.261	1.65	0.261	2.86	0.535	**1.1**	0.537	31.0	**0.137**	5.87	2.24	
Bolivia	Paleozoic	34.3	71.6	8.71	32.5	6.54	1.26	5.42	0.939	5.46	1.11	3.25	0.487	3.10	0.466	8.18	1.14	**1.5**	0.614	20.2	**0.210**	13.9	4.38	
Dwyka East	Paleozoic	44.2	90.2	10.7	39.7	7.90	1.49	6.38	1.07	5.95	1.21	3.52	0.518	3.27	0.499	6.77	0.991	**0.88**	0.667	25.8	**0.209**	16.9	3.29	
Dwyka West	Paleozoic	19.3	40.0	5.00	18.3	3.65	0.83	3.05	0.516	2.91	0.615	1.85	0.277	1.79	0.274	2.51	0.519	**1.2**	0.635	7.95	**0.189**	5.91	1.91	

Note: Results for individual samples are provided in Supplemental Table B.1. Boldfaced values were determined by standard addition ICPMS.

* XRF conducted at Franklin and Marshall College. Major elements have been normalized to equal 100% upon inclusion of LOI.

** LOI = lost on ignition.

*** CIA = chemical index of alteration ($Al_2O_3/Al_2O_3 + CaO^* + K_2O + Na_2O$) where CaO has corrected to remove contributions from apatite and carbonates.

**** M, W, and F are mafic, weathered, and felsic endmembers based on the principal component analysis approach of Ohta and Arai (2007).

° ICPMS analyses conducted at University of Maryland.

°° Zn values are from XRF.

prepared using 0.5 mL of master solution, adding 0.5 mL of an indium standard solution (as an internal drift corrector), and diluting to 15 mL with 2% HNO_3 containing a trace of HF to prevent precipitation of the highly insoluble high field strength elements. The second dilution was prepared by taking 1 mL of the first solution and diluting this to 7.5 mL with 2% HNO_3. The dilutions were analyzed within 24 h of preparation in order to avoid precipitation of elements having low solubilities.

2.3.2. ICP-MS protocols

Most samples were analyzed for trace elements on a Thermo-Finnigan Element 2 high resolution-ICP-MS in the Department of Geology at the University of Maryland. Instrumental parameters are given in Supplemental Table A.1. Samples were analyzed with aliquots of USGS whole-rock standards AGV-2, BHVO-1, GSP-1, and W-2 that were prepared at the same time as the samples. Elemental concentrations in samples were determined by constructing calibration curves with the four USGS standards. Precision and accuracy were evaluated by repeated analysis of separately dissolved AGV-2 aliquots treated as unknowns and are reported in Table 3. Precision was better than 4% relative standard deviation (1σ) for the majority of elements. Results for individual samples are reported in Supplemental Table B.1, and results for composites are reported in Table 2.

Table 3
Precision and reproducibility based on analysis of AGV-2 as an unknown.

	Average $(n = 7)$[*]	1 std	%RSD	GEOREM	Average/GEOREM	Std add value[**] $(n = 6)$	Std add %RSD
Li	11.5	0.3	3.0	11	1.05		
Be	2.28	0.09	4.0	2.3	0.99		
Sc	12.6	1.6	12.9	13	0.97		
V	122	7	6.0	120	1.02		
Cr	15.5	0.5	2.9	17	0.91		
Co	15.2	0.3	1.8	16	0.95		
Ni	19.1	0.4	2.0	19	1.00		
Cu	52.8	1.4	2.6	53	1.00		
Ga	20.4	0.3	1.5	20	1.02	20.2	2.0
Ge	1.22	0.043	3.5	1.43	0.86	1.15	3.4
Rb	66.2	0.5	0.8	66.3	1.00		
Sr	649	5	0.7	661	0.98		
Y	20.2	0.2	1.1	20	1.01		
Zr	230	17	7.2	240	0.96		
Nb	13.8	0.2	1.4	14.6	0.95		
Mo	2.21	0.25	11.2	2.08	1.06	1.93	2.4
Cd[***]				0.0820		0.137	3.6
In[***]				0.0480		0.0445	2.0
Sn	2.14	0.45	21.1	2.08	1.03	1.90	3.2
Sb	0.469	0.021	4.5	0.5	0.94	0.574	8.1
Cs	8.83	0.07	0.8	7.57	1.17		
Ba	1133	14	1.2	1140	0.99		
La	40.2	0.3	0.9	37.9	1.06		
Ce	73.1	0.5	0.7	68.6	1.07		
Pr	8.83	0.07	0.8	7.57	1.17		
Nd	32.2	0.2	0.7	30.2	1.06		
Sm	5.93	0.07	1.2	5.49	1.08		
Eu	1.62	0.02	1.1	1.53	1.06		
Gd	4.58	0.05	1.1	4.52	1.01		
Tb	0.694	0.008	1.1	0.64	1.08		
Dy	3.60	0.05	1.3	3.47	1.04		
Ho	0.710	0.009	1.3	0.653	1.09		
Er	1.93	0.02	1.2	1.81	1.06		
Tm	0.272	0.003	1.0	0.26	1.05		
Yb	1.68	0.04	2.3	1.62	1.04		
Lu	0.257	0.003	1.3	0.247	1.04		
Hf	5.65	0.16	2.7	5.04	1.12		
Ta	0.907	0.040	4.4	0.89	1.02		
W	0.651	0.107	16.4	0.55	1.18	0.489	4.2
Tl	0.317	0.003	1.1	0.32	0.99	0.272	5.6
Pb	15.9	0.4	2.3	14.2	1.12		
Bi	0.0431	0.0103	23.9	0.052	0.83	0.0509	9.0
Th	6.62	0.17	2.6	6.16	1.07		
U	2.07	0.05	2.5	1.9	1.09		

[*] Average values for analysis by conventional external calibration with USGS standards.
[**] Average values for standard addition analysis.
[***] Cd and In were determined by standard addition only.

A small subset of samples (those from the Konnarock, Nantuo and Gucheng formations) were analyzed on an Agilent 7700x quadrupole ICP-MS in the State Key Laboratory for Geological Processes and Mineral Resources at the China University of Geoscience in Wuhan, China and these are shown in italics in Supplemental Table B.1, along with the samples analyzed at the University of Maryland. Instrumental parameters are given in Supplemental Table A.1. Calibration was conducted using multi-element standard solutions to create a calibration line, and then adjusting this calibration after analysis of dissolved whole-rock standards. Precision and accuracy are discussed in Hu and Gao (2008).

2.3.3. Standard addition analysis

A subset of samples was analyzed by standard addition ICP-MS at the University of Maryland for Ga, Ge, Mo, Cd, In, Sn, Sb, W, Tl, and Bi, since the concentrations of these elements are relatively poorly constrained in the whole-rock standards used for calibration. Two spikes were prepared from single-element standard solutions, one containing Ga, Ge, Mo, Sn, and W, and one containing Cd, In, Sb, Tl, and Bi. These two spikes were prepared due to the large difference in concentrations found in typical crustal rocks and the potential for polyatomic interferences between the groups (e.g., Mo-oxides on Cd). Four solutions were analyzed per sample (for a given spike) consisting of: (1) a total analytical blank; (2) an unspiked aliquot of sample; (3) a spiked aliquot of sample; and (4) an aliquot of a sample spiked with twice the volume of spike as the previous one. All aliquots were also spiked with a Rh solution, which was used for internal drift correction. Precision and accuracy of this method based on analyses of AGV-2 as an unknown are presented in Table 3. Further details of this approach, including data for other standard reference materials, are given in Gaschnig et al. (2015a).

2.4. Oxygen isotope analysis

Whole-rock powders were analyzed for oxygen isotope ratios at the University of Wisconsin-Madison by laser fluorination (Valley et al., 1995) using an air-lock sample chamber (Spicuzza et al., 1998) with BrF_5 as a reagent and a 25 W CO_2 laser ($\lambda = 10.2\ \mu m$). By this means, 2–3 mg samples of powder were outgassed at vacuum overnight and fluorinated individually so as to prevent cross-contamination. Evolved oxygen was cryogenically cleaned, passed through heated Hg vapor, and converted to CO_2 over hot graphite for analysis. Isotope ratios were measured on a Finnigan MAT 251 dual inlet mass spectrometer and are reported in standard permil notation relative to VSMOW (Vienna Standard Mean Ocean Water). Measured values were standardized using the UWG-2 garnet standard ($\delta^{18}O = 5.80\%o$ VSMOW; Valley et al., 1995). Overall reproducibility of the standard during the analytical sessions was $\pm 0.18\%o$ (2 SD). Results are given in Supplemental Table B.1.

3. RESULTS

3.1. Major elements

The major element compositions of siliciclastic sediments such as diamictites reflect the relative proportions of quartz to feldspars and clays/phyllosilicates, and the majority of diamictites falls along the expected mixing trend in a plot of SiO_2 vs. Al_2O_3 (Fig. 1a). Several samples deviate from this trend and are characterized by either unusually high CaO or Fe_2O_3(T) (Fig. 1b and c). Although these outlier samples encompass all four age groups, they all share a common origin in southern Africa. The high CaO samples also have high LOI values (see Supplemental Fig. A.2), consistent with high levels of carbonate. The high levels of carbonate and Fe have a dilution effect on the other major elements.

3.2. Trace elements

Trace element concentrations are plotted in Figs. 2–4, organized by element groups. In order to account for the effects of dilution from quartz, carbonate, or Fe on absolute abundances of trace elements (see above), samples are first normalized to the average UCC abundance of Al_2O_3 (15.26%) of Rudnick and Gao (2003). Aluminum is used for this purpose because it is an immobile element with a relatively restricted range in crustal igneous rocks (i.e., both basalts and granites commonly have ~15 wt% Al_2O_3). This normalization is done by dividing 15.26 by the measured Al_2O_3 in each sample, which results in a value greater than one for this "adjustment factor" in samples that are affected by quartz, carbonate, or Fe dilution. We then multiply the concentrations for each trace element by the adjustment factor. Data for individual elements are then normalized to the average UCC of Rudnick and Gao (2003) (hereafter referred to as UCC_{RG}) (with the exception of the chondrite normalized left half of Fig. 2), which provides a frame of reference. For the sake of clarity, only composites are plotted in Figs. 2–4. This is justified by the close comparison between the calculated medians of individual samples for a given formation and their composites. Further comparison of the individual sample results to the composites is shown in Supplemental Fig. A.1.

3.2.1. Rare earth elements (REE)

The REE are incompatible, insoluble lithophile elements that show a systematic increase in compatibility with increasing atomic number, with the exception of Eu, which mirrors the behavior of Ca and Sr when in a 2+ oxidation state. REE patterns, including Y (which behaves like a heavy REE and is plotted between Ho and Er), are shown in Fig. 2. The diamictites all show chondrite-normalized REE patterns (Fig. 2a) that are characterized by light REE (LREE)-enrichment and negative Eu anomalies (Eu anomaly or $Eu/Eu^* = (Eu/(Gd*Sm)^{0.5}$, with all concentrations normalized to chondrite), save one Mesoarchean sample that has a positive Eu anomaly. Differences are more apparent when the results are normalized to UCC_{RG} (Fig. 2b). Three of the Mesoarchean composites have
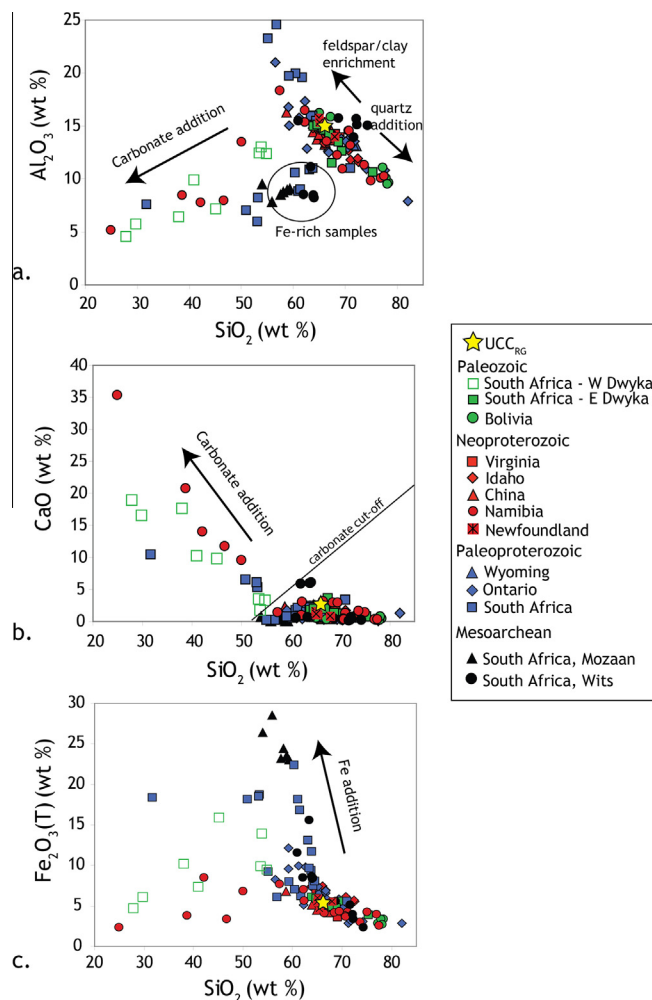
Fig. 1. Diamictite major element compositions (and sediments in general) are chiefly controlled by the ratio of quartz to feldspars and clays/phyllosilicates, which forms the primary trend. Departures from this trend are caused by unusually high levels of either $CaCO_3$ or iron, as seen in (b) and (c), which cause relative dilutions in the other major elements. The "carbonate cut-off" line in (b) separates the carbonate-rich samples on the left from those used to calculate the filtered medians in Figs. 13 and 14.

normalized REE abundances and LREE to heavy rare earth element (HREE) fractionation similar to that of UCC_{RG}, whereas the fourth is depleted in the LREE but not the HREE relative to UCC_{RG}. All Archean composites are enriched in Eu relative to UCC_{RG}. The majority of the Paleoproterozoic composites show normalized concentrations and LREE to HREE fractionation comparable to UCC_{RG}, whereas Eu may be slightly enriched or depleted relative to UCC_{RG}. The Neoproterozoic composites differ from the older ones in that many show a positive slope when normalized to UCC_{RG}, indicating less fractionation between the LREE and HREE, and all are Eu depleted. In addition, the Neoproterozoic Idaho composite is distinctly more enriched in all REE than the other composites of all ages. The Paleozoic composites are indistinguishable from the Neoproterozoic composites, although Dwyka West has lower overall abundances and is not depleted in Eu.

3.2.2. Transition and post-transition metals and metalloids

The transition metals are generally compatible, may exhibit multiple valence states, and may show lithophile,

chalcophile, and/or siderophile characteristics. The post-transition metals and metalloids exhibit both compatible and incompatible behavior and are primarily chalcophile. The transition metal concentrations change as a function of the age of the sediment (Fig. 3a). Mesoarchean composites are generally enriched in all transition metals relative to UCC_{RG} but the enrichment is significantly greater for Cr and Ni relative to the other metals. Paleoproterozoic composites show mild enrichment in Cr, but otherwise are similar to UCC_{RG}. Neoproterozoic composites are generally depleted in Cr, Co, and Ni but show similar Sc and V concentrations to UCC_{RG}. Of the Paleozoic composites, the western Dwyka shows significant enrichment in all transition metals, comparable to the Mesoarchean composites. The other Paleozoic composites have transition metal levels overlapping those of the Neoproterozoic composites and similar to UCC_{RG}.

The post-transition metals and metalloids are plotted, along with transition metals Cu and Zn, in Fig. 3b. Copper concentrations vary more than those of all other elements (roughly two orders of magnitude). Although the
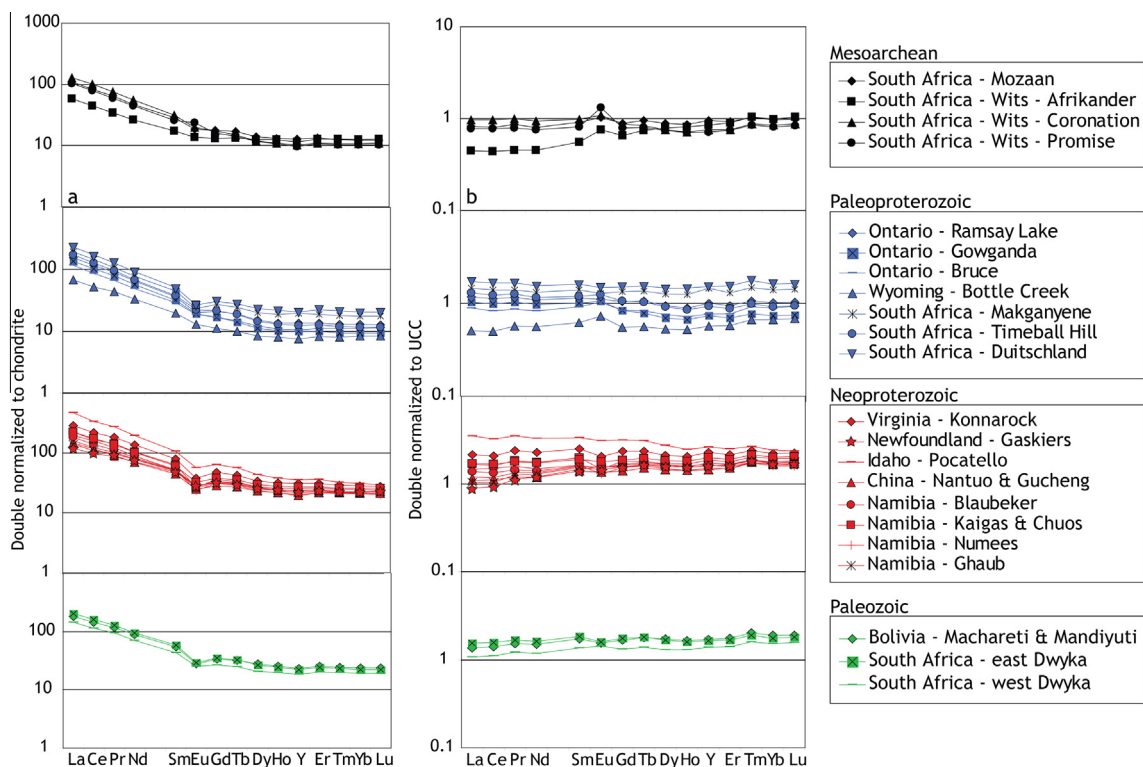
Fig. 2. Rare earth element (REE) variations in diamictite composites ordered by depositional age. Measured concentrations are double-normalized, with each analysis corrected for quartz dilution by normalizing it to the average UCC_{RG} Al_2O_3 content and then normalizing individual elements to chondrite (McDonough and Sun, 1995) in panel a, and average UCC_{RG} in panel b.
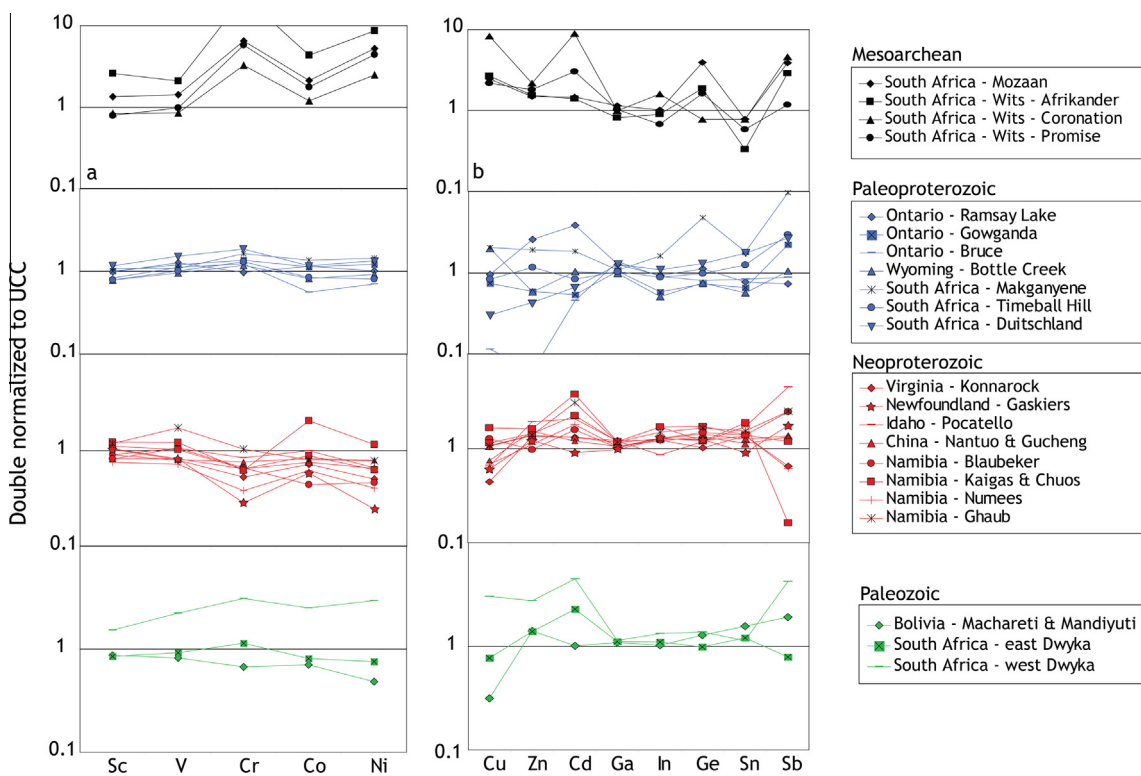

Fig. 3. Transition metals (a) and post-transition metals and metalloids (b) in diamictite composites, double normalized to UCC_{RG}, as in Fig. 2.
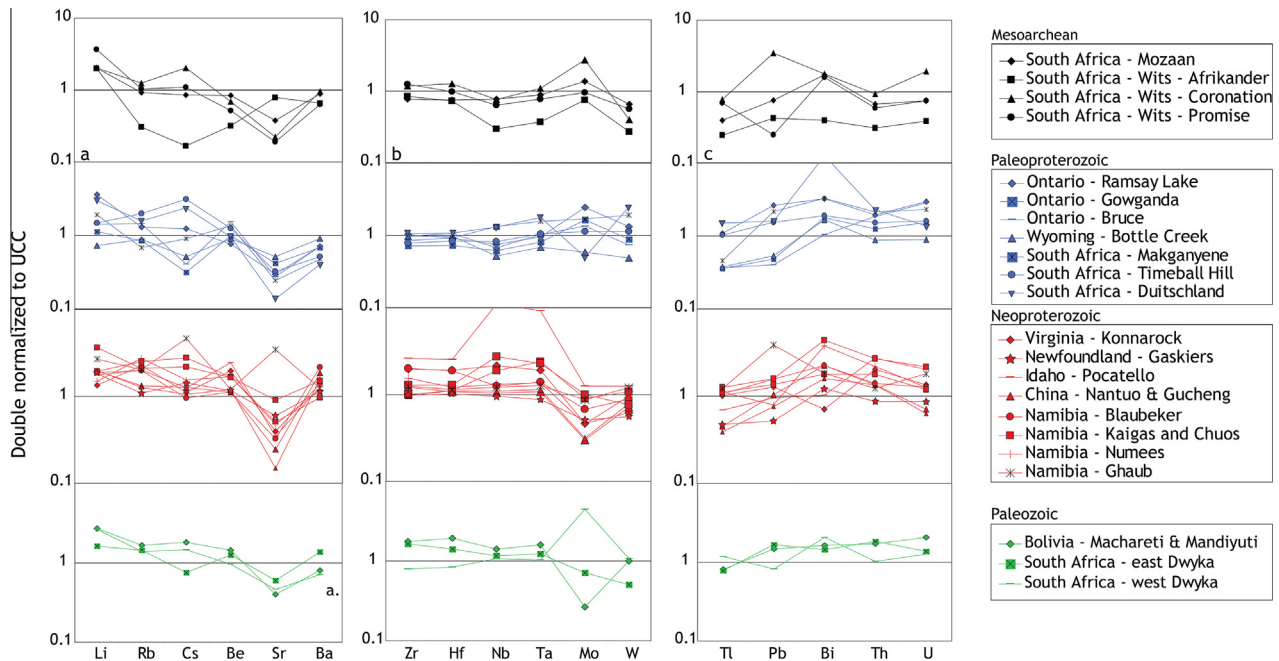
Fig. 4. Alkali and alkaline earth elements (a), high field strength elements (HFSE; b), and actinides (c) in diamictite composites, double normalized to UCC_RG, as in Fig. 2.

Mesoarchean composites are all enriched in Cu, the younger composites show both enrichment and depletion relative to UCC_RG. Paleoproterozoic composites are particularly notable for the large range of normalized Cu concentrations observed. Zinc is also quite variable in the Paleoproterozoic composites, but composites from other periods show a narrower range of concentrations and are consistently enriched relative to UCC_RG. Cadmium also shows significant variability but tends to be enriched in most composites relative to UCC_RG. Compared to all other post-transition metals, concentrations of Ga and In, which belong to the same group as Al on the Periodic Table, show little variability and match UCC_RG estimates. Germanium concentrations vary widely, especially in the Paleoproterozoic and Mesoarchean composites, and are both enriched and depleted relative to UCC_RG; there is no correlation between Ge and SiO_2 contents. Tin is depleted relative to UCC_RG in the Mesoarchean and some of the Paleoproterozoic composites, but is enriched in all other composites. Antimony concentrations are highly variable in diamictites of all time periods, and show no obvious trend with age, but tend to be enriched in the diamictites relative to UCC_RG.

3.2.3. Alkali and alkaline earth elements

The alkali and alkaline earth elements are incompatible and relatively soluble lithophile elements; their normalized concentrations in the diamictite composites are shown in Fig. 4a. Lithium is enriched relative to UCC_RG in nearly all composites, and Rb is generally enriched in all post-Archean samples. Cesium is highly variable, showing both large enrichments and depletions in different composites with no obvious trend with age. Beryllium concentrations appear to increase with age. Strontium is depleted relative

to UCC_RG in all composites save the carbonate-rich Neoproterozoic Ghaub Formation. Barium concentrations show a relatively narrow range in the diamictites, with some suggestion of an increasing concentration over time with respect to UCC_RG.

3.2.4. High field strength elements (HFSE)

The HFSE are incompatible and primarily lithophile elements, although Mo and W may show chalcophile and siderophile characteristics, respectively. Normalized HFSE concentrations for the composites are shown in Fig. 4b. Zirconium and Hf concentrations show limited variability and are close to UCC_RG, with the exception of the Neoproterozoic Pocatello (Idaho) and Blaubeker formations that are enriched in Zr and Hf. Niobium and Ta concentrations vary more widely and show an increase with time relative to UCC_RG. Several Neoproterozoic composites show significant enrichment in Nb and Ta, and the enrichment is especially large (∼10 times UCC_RG) in the Pocatello composite. Molybdenum concentrations show significant variability within and between the different time periods, but are generally higher in the Mesoarchean and Paleoproterozoic than the Neoproterozoic and Paleozoic, with the exception of the Mo-enriched western Dwyka composite. Tungsten concentrations are depleted in the Mesoarchean and Neoproterozoic composites relative to UCC_RG, but are similar to or enriched relative to UCC_RG in the Paleoproterozoic and two of the three Paleozoic composites.

3.2.5. Heavy post-transition metals and actinides

The heavy post-transition metals (Tl, Pb, and Bi) (Fig. 4c) are incompatible elements with both lithophile and chalcophile characteristics. The actinides (Th and U)

are incompatible lithophile elements. Concentrations of all five elements vary widely in the composites of all periods except the Paleozoic. Thallium is either similar to or depleted relative to UCC_{RG} in all periods. Lead concentrations are either higher or lower than UCC_{RG} and show no temporal trend. Bismuth concentrations are enriched relative to UCC_{RG} for most composites. Thorium and U concentrations are depleted in the Mesoarchean but enriched in the other periods. Th/U increases systematically from the Mesoarchean, which has lower Th/U than UCC_{RG}, to the Neoproterozoic, which has higher Th/U than UCC_{RG}. By contrast, Th/U of the Paleozoic samples are similar to UCC_{RG}.

3.3. Oxygen isotopes

Fig. 5a shows the $\delta^{18}O$ values for individual glacial diamictite powders as a function of age, after filtering the data set to exclude samples with LOI values greater than 7%. (We exclude these samples to eliminate the effects of carbonate, which leads to abnormally high $\delta^{18}O$ values. See Supplemental Fig. A.2 for justification of this cut-off criterion). The oxygen isotope ratios of the diamictites tend to become heavier and more variable with time. Values of $\delta^{18}O$ are the lowest in the Archean diamictites, which overlap with the modern mantle. Most of the Paleoproterozoic diamictites have $\delta^{18}O$ values that overlap with those of the higher $\delta^{18}O$ Archean diamictites, but diamictites from the

Makganyene and Duitschland formations from South Africa have considerably higher $\delta^{18}O$, ranging from 13‰ to 18‰. The majority of Neoproterozoic samples have values between 10‰ and 15‰. Several of the Paleozoic samples overlap with the main Neoproterozoic group but a few samples have lower $\delta^{18}O$ values.

Fig. 5b shows $\delta^{18}O$ of the diamictites versus their chemical index of alteration values (CIA = molar $Al_2O_3/(Al_2O_3 + CaO^* + K_2O + Na_2O)$, where CaO^* is corrected for apatite and carbonate; carbonate correction using approach of McLennan, 1993) (Nesbitt and Young, 1982), which are a measure of chemical weathering intensity (see below). While a positive correlation is present for the Neoproterozoic and Paleozoic diamictites, $\delta^{18}O$ and CIA are largely decoupled in the older diamictites. In particular, the Mesoarchean samples have very high CIA but mantle-like $\delta^{18}O$.

4. DISCUSSION

The efficacy of using glacial diamictites to track changes in the average UCC composition is contingent upon two main factors. First, the diamictites must preserve the original composition of the eroded crustal material without being significantly modified by syn- or post-depositional processes such as chemical weathering. Second, the diamictites must consist of material pulverized by ice sheets from large continental areas, as opposed to preferentially
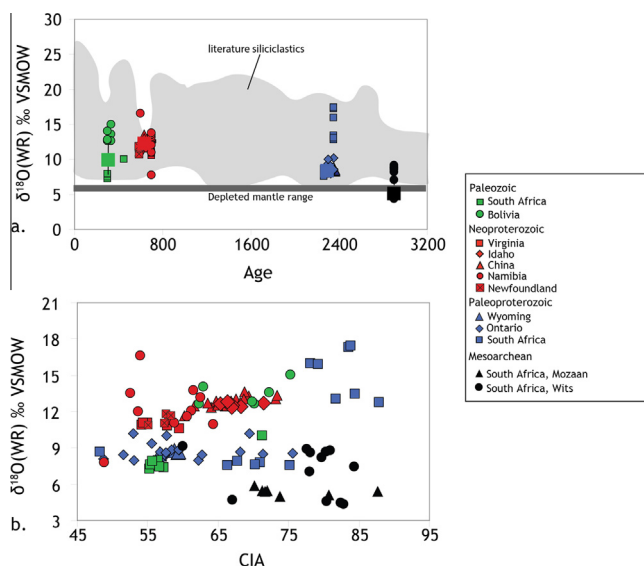

Fig. 5. (a) Whole-rock oxygen isotope compositions of individual diamictite samples versus depositional age. Diamictites with LOI values greater than 7% were excluded in order to eliminate the skewing effects of high carbonate content on $\delta^{18}O$ (see Supplemental material for discussion). Large colored boxes are median values for each of the four time periods. The median absolute error is shown as a vertical line for the Paleozoic but is smaller than the symbols for the other three periods. Mantle composition is from Valley et al. (1998). Shaded field is range of clastic sediment/sedimentary rock analyses compiled by Payne et al. (2015), filtered here to exclude samples metamorphosed at medium and high-grade conditions, with additional data from Bindeman et al. (2016). Mesoarchean diamictites extend to distinctly lower $\delta^{18}O$ values compared to post-Archean diamictites. Although the other three glacial periods contain outliers, the average values become progressively higher with time. (b) $\delta^{18}O$ versus CIA (chemical index of alteration, a measure of chemical weathering intensity). If $\delta^{18}O$ values are being controlled by chemical weathering, a positive correlation should be present in the data. While this is true of the Neoproterozoic and Paleozoic diamictites, the $\delta^{18}O$ and CIA values are largely decoupled for the Mesoarchean and Paleoproterozoic diamictites. (For interpretation of the references to color in this figure legend, the reader is referred to the web version of this article.)

sampling local sources near the ice sheet terminus. We consider these two factors below, and then discuss evidence in the diamictites for secular changes in the average UCC composition and finally, use our new data to derive an average UCC composition, along with uncertainties, and compare that with previous results.

4.1. Identifying and seeing through the effects of chemical weathering

Sediments and sedimentary rocks frequently show the effects of chemical weathering, which obscures information about the bulk composition of their sources. Several geochemical indices have been used to recognize chemical weathering effects, the most popular of which is the chemical index of alteration. Fresh igneous rocks have CIA values ranging from 40 to 55 and pure kaolinite and chlorite have a value of 100, owing to their lack of Ca, Na, and K. Gaschnig et al. (2014) noted that the majority of diamictites have CIA values elevated above those of igneous rocks; they also attributed the pervasive Sr depletion seen in the diamictites to the influence of chemical weathering. This weathering signature appears to be inherited from the sediment source in most cases, rather than reflecting post-depositional changes or weathering during glacial erosion and transport (Gaschnig et al., 2014; Li et al., 2016).

A weakness of using the CIA value to assess chemical weathering effects is its inability to take into account the original bulk composition of the protolith. This is especially problematic at low CIA because unweathered igneous rocks can show a range of CIA values: basalts tend to have the lowest CIA, around 40, whereas granites have higher CIA, up to 55. One way of extracting information on source lithologies from major element data of sedimentary rocks that show the influence of chemical weathering is to pair the CIA value with another index called the ICV (index of chemical variability) (Cox et al., 1995), which is defined as $ICV = (TiO_2 + Fe_2O_3(T) + MnO + MgO + CaO + K_2O + Na_2O)/Al_2O_3$ (with all oxides as weight percent). ICV values are higher for more mafic source lithologies and when plotted against CIA values (Fig. 6) (Potter et al., 2005), straight lines connecting a completely weathered end member (pure kaolinite/chlorite) to average igneous compositions reflect weathering trends. The majority of the diamictite data plot on a broad weathering trend consistent with an average andesitic source region, which is close to the expected granodioritic average composition of the UCC. However, many Mesoarchean and Paleoproterozoic samples fall along trends suggestive of a basaltic or komatiitic average source composition, indicating that the UCC from these earlier time periods was more mafic.

Another method used for separating source composition from weathering effects in sedimentary rocks was developed by Ohta and Arai (2007). This approach uses principle component analysis to assign and weight all major element oxides into mafic (M), felsic (F), and weathered (W) end members. Individual diamictites are plotted in this framework in Fig. 7. As in Fig. 6, the majority of samples plot
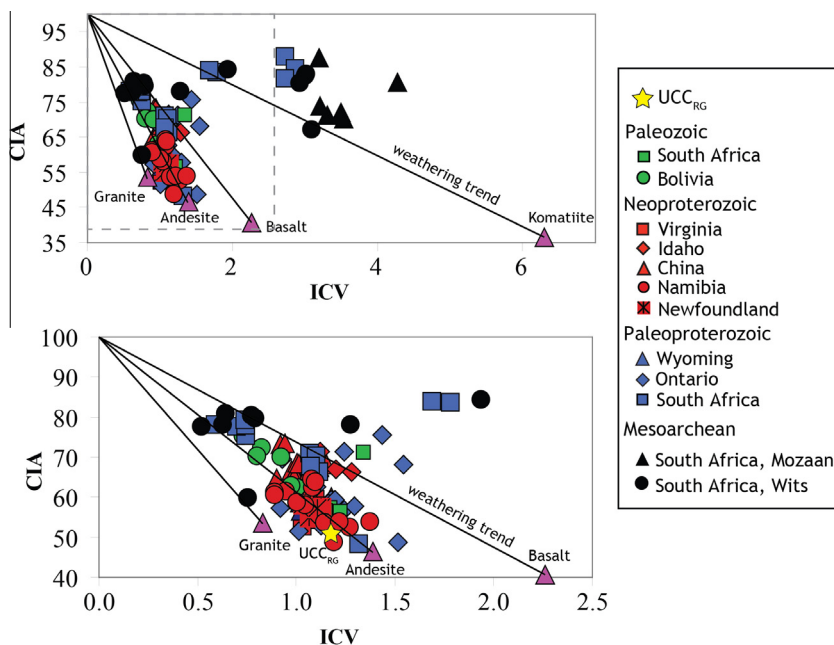

Fig. 6. Upper: Chemical index of alteration (CIA) versus index of chemical variability (ICV). Lower: an expanded view of the dashed box in the upper panel. The ICV increases as the composition becomes more mafic. See text for formal definitions. Average igneous compositions shown as purple triangles are from Condie (1993) and tie lines to CIA = 100 and ICV = 0 are weathering trends. UCC$_{RG}$ is also shown as a purple triangle and plots with a primary igneous CIA because it is largely derived from grid sampling studies of igneous basement. Samples with >7% LOI have been excluded, as their high carbonate content results in extreme ICV values. Most diamictites fall along a weathering trend leading back to an andesitic composition, but many of the Mesoarchean and some of the Paleoproterozoic samples fall near tie lines more consistent with a komatiitic source. (For interpretation of the references to color in this figure legend, the reader is referred to the web version of this article.)
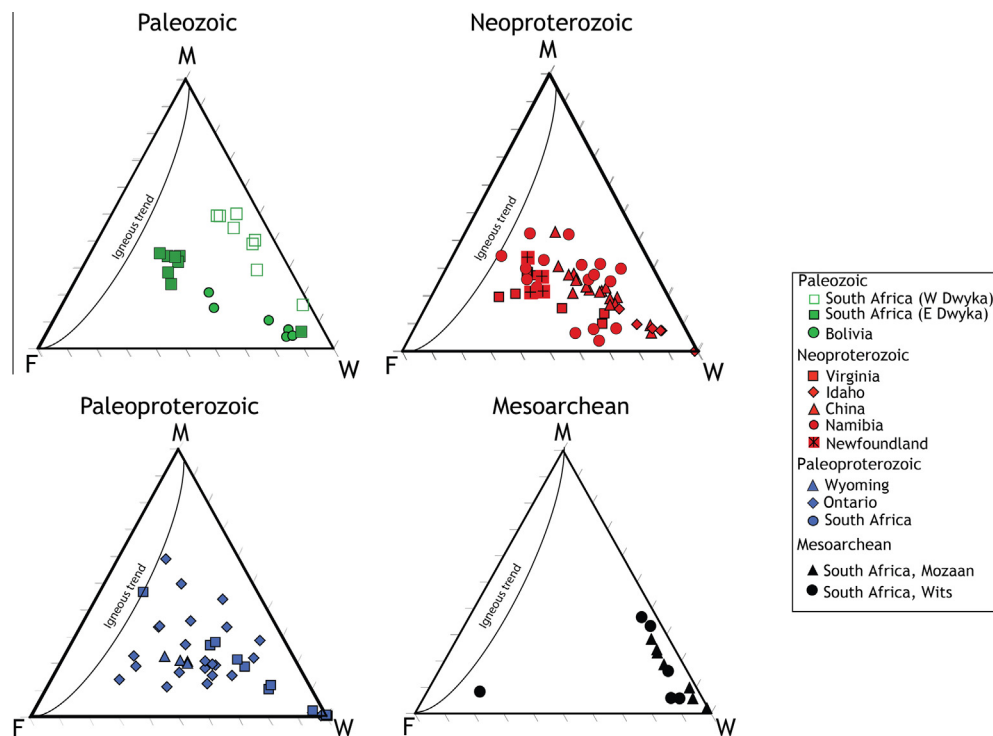
Fig. 7. Ternary plots separating the effects of weathering from source rock composition, after Ohta and Arai (2007). This approach is based on principal component analysis of the major elements and divides compositions among "mafic" (M), "felsic" (F), and "weathered" (W) end-members. Unweathered igneous rocks plot along the arc connecting the M and F apices whereas weathering will draw compositions toward the W apex. Most diamictites plot in positions consistent with a weathered intermediate source composition but Mesoarchean samples clearly derive from a more mafic source.

in a broad field reflecting a weathering trend projecting to intermediate composition igneous protoliths, except for a select group of Paleozoic Dwyka samples (the west Dwyka) and nearly all of the Archean samples. These samples form a weathering trend that projects to a mafic igneous protolith. Thus, although the diamictites all bear chemical weathering signatures of various intensities, it is possible to use their major elements to identify a major change in the nature of the crust being weathered and eroded between the Archean and Paleoproterozoic.

4.2. Identifying and seeing through the effects localized or non-representative provenance

Research on modern and Pleistocene glacial erosion and sedimentation has shown that large ice sheets are capable of transporting sediment great distances, but that sediment from upstream sources may become diluted by material from nearby sources with increasing downstream distance (e.g., Clark, 1987; Klassen, 1999; Hildes et al., 2004; Farmer et al., 2006). Dispersal distance appears to be controlled primarily by basal ice velocity and bedrock topography (Clark, 1987). The effects of localized provenance are seen on the geochemistry of some of the diamictites. The two most prominent examples are found in the Pocatello Formation and Dwyka Group. Diamictites from the Neoproterozoic Pocatello Formation are unusually enriched in Nb and Ta (by an order of magnitude relative to

UCC_{RG}, Fig. 4b) and the REEs, especially the LREEs (enriched by a factor of two relative to UCC_{RG}, Fig. 2). These enrichments reflect the contribution from local Neoproterozoic bimodal alkaline volcanic rocks formed during the rifting of Rodinia, which are strongly enriched in these elements (Yonkee et al., 2014). The influence of these alkaline rocks is supported by the large number of detrital zircons of the appropriate age found in this diamictite (Yonkee et al., 2014), and the high concentrations of Zr and Hf (Fig. 4b). Despite this clear local signature, the Pocatello Formation also shares distinctive chemical characteristics that are common to all Neoproterozoic diamictites, such as the depletion of V, Sc, Mo, and especially Cr and Ni relative to REE.

Another example of the influence of localized provenance is found in the Dwyka Group, where major geochemical differences exist between diamictites collected in separate parts of the Karoo Basin. Samples from the western Dwyka have significantly higher concentrations of the compatible transition metals (Sc, V, Cr, Co, Ni, Cu, Zn, Mo, Cd) and lower concentrations of the REE than samples from the southeastern Dwyka. These chemical characteristics appear to reflect differences in provenance governed by ice flow directions. Detrital zircons from the west Dwyka samples are 2.0 Ga and older (Gaschnig et al., 2015b), indicating that the ice in this region was exclusively sampling the Archean interior of the Kaapvaal craton (plus the Paleoproterozoic Bushveld Complex). By

contrast, a large diversity of detrital zircon ages, ranging from Early Paleozoic to Archean, are found in the southeastern portion of the Dwyka Group (Vorster, 2013), indicating both a greater diversity of sediment sources and a dominance of Mesoproterozoic and younger ages. Thus, the transition metal enrichments (Fig. 3a) and the major element evidence for a much more mafic source rock (Fig. 7) for the west Dwyka diamictites relative to the remainder of the Dwyka samples both reflect sampling of Archean crust by the Paleozoic glaciers in the west.

Despite the influence of localized provenance seen in the geochemistry of certain samples discussed above, there are common geochemical features seen globally among similarly aged samples. This is especially apparent for elements such as the REE, which show similar fractionation patterns and abundances for each time period, and the transition metals, which show relatively uniform levels of enrichment or depletion in each time period. Furthermore, many of the other diamictites for which detrital zircons have been dated show age spectra with a wide range of ages, indicating a diversity of sediment sources (e.g., Liu et al., 2008; Hofmann et al., 2015). Consequently, the majority of the diamictites appear to consist of sediments drawn from large continental areas, making them reliable proxies for the average UCC for many elements. We next explore the key geochemical features seen among diamictites of different ages.

4.3. Secular changes in diamictite compositions

Systematic secular changes in the compositions of the diamictites are observed that reflect changes in the average composition of the UCC through time. We explore these changes below in plots of elemental ratios versus age for insoluble elements in the composite samples (Figs. 8 through 12), and measure the robustness of these changes through statistical analysis. We used Kolmogorov–Smirnov tests and normality plots to determine if variables met the assumptions of a parametric test and log transformed the ratios when necessary to improve normality. We used MANOVA (multivariate analysis of the variance) to compare normally distributed ratios among the four time periods and used post hoc univariate ANOVAs and Tukey tests to identify significant differences among periods. All tests were two-tailed and we set $\alpha = 0.05$. For ratios that were not normally distributed, we used a Kruskal–Wallis test to compare ratios among the different time periods. Analyses were performed in PASW 18 (SPSS). Results are provided in the Supplemental Tables A2 and A3. All of the element ratios examined differed significantly among the four time periods (all $p < 0.05$), with the exception of Gd/Lu.

4.3.1. Evidence for increasingly differentiated and felsic UCC with time

As noted above, techniques using major element composition to separate sediment source from weathering effects reveal that the Mesoarchean and some of the Paleoproterozoic diamictites have distinctly more mafic provenances that include komatiites (Figs. 6 and 7). Moreover, from

the Archean to the present, diamictites show a secular decrease in the abundance of the compatible first row transition metals (Sc, V, Cr, Co, and Ni, Fig. 3), a feature also documented in Fig. 4 of Gaschnig et al. (2014). These transition metals are contained primarily in mafic minerals, and the depletion of these elements with decreasing age is consistent with the UCC becoming less mafic with time. We can summarize this observation using the Ni/Lu ratio plotted against deposition age (Fig. 8a), where Lu is used as a reference element having limited absolute variation (in the same way that Al is used in the multi-element plots in Figs. 2–4). Ni/Lu ratios in Mesoarchean diamictites are distinctly higher than all other composites, demonstrating that these diamictites were sourced from a UCC with high Ni content. Diamictites from the post-Archean glaciations show successively lower Ni/Lu ratios (with the exception of the western Dwyka samples previously discussed). These observations are consistent with the UCC being more mafic in the Archean and becoming progressively more differentiated and felsic in composition with time (Tang et al., 2016).

The Th/Sc ratio is used to differentiate between mafic and felsic provenance of sediments, given the compatibility of Sc and the incompatibility of Th in igneous systems (e.g., Taylor and McLennan, 1985). Sediments from granitic source rocks thus have higher Th/Sc ratios than those from basaltic source rocks. The Mesoarchean diamictite composites show the lowest Th/Sc ratios, which is consistent with the other lines of evidence indicating a predominantly mafic source (Fig. 8b). In contrast to the continuous change with time seen in the Ni/Lu ratio, the Th/Sc ratio increases between the Mesoarchean and Paleoproterozoic but does not show a continuous secular trend.

The Eu/Eu* ratio is another measure of intracrustal differentiation. This is because Eu^{2+} enters feldspar relative to Eu^{3+}, which leads to the development of a negative Eu anomaly (Eu/Eu* < 1) in evolved magmas derived from melting or differentiation within the crust of typical thickness ($\leqslant 35$ km) (e.g., Taylor and McLennan, 1985; Rudnick and Gao, 2003; Tang et al., 2015). As with the Ni/Lu ratios, the diamictites show a continuous decrease in Eu/Eu* with time (Fig. 8c). This suggests that intracrustal differentiation became increasingly important through time and is consistent with a greater proportion of mafic, undifferentiated magmas making up the bulk of the Archean UCC.

The oxygen isotope compositions of the diamictites likely reflect the original $\delta^{18}O$ of the provenance, which, in turn, reflects its chemical weathering or alteration history. Low temperature interactions with water at or near the Earth's surface drives the oxygen isotopic compositions of rocks toward higher $\delta^{18}O$ values, starting from the mantle $\delta^{18}O$ value of $5.6 \pm 0.3‰$ (Mattey et al., 1994; Valley et al., 1998; Eiler, 2001; Grimes et al., 2011). As noted above, the $\delta^{18}O$ of the diamictites generally increase with time (Fig. 5a). The oxygen isotope composition of Mesoarchean diamictites have both relatively low $\delta^{18}O$ values and a limited range (Fig. 5a). These samples overlap in part with the $\delta^{18}O$ composition of the modern mantle and are lower, on average, than the published values for Archean siliciclastic sediments compiled by Payne et al.
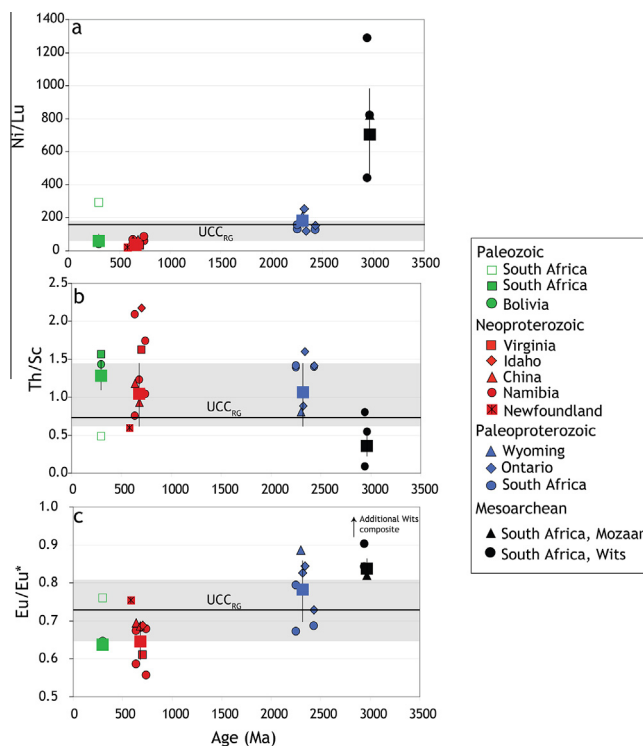
Fig. 8. Trace element ratios sensitive to differentiation and/or mafic versus felsic sources plotted against depositional age for the composites, which represent average compositions for each diamictite unit. The decreasing (a) Ni/Lu, increasing (b) Th/Sc, and increasingly negative Eu anomaly (c) are all consistent with a progressively less mafic, more differentiated UCC with time. Large boxes and vertical bars represent median values and median absolute deviations for all individual samples from each time period, with the exception of the western Dwyka samples, which are dominated by >2.0 Ga sources (see text for discussion). In this and subsequent figures, the UCC$_{RG}$ line represents the average UCC composition of Rudnick and Gao (2003) and shaded area represents the range of other published UCC models (Shaw et al., 1967, 1976; Eade and Fahrig, 1973; Taylor and McLennan, 1985; Condie, 1993; Wedepohl, 1995; Gao et al., 1998; Kamber et al., 2005; Hu and Gao, 2008; Chauvel et al., 2014).

(2015) and Bindeman et al. (2016). The δ^{18}O values of the Archean diamictites are also decoupled from the CIA values, which are high (~70–90) (Fig. 5b). The persistence of the low Archean δ^{18}O values suggests either that weathering processes did not significantly contribute to their oxygen isotope compositions, or that Archean surface waters had a significantly different oxygen isotope composition than today (Muehlenbachs, 1998; Knauth and Lowe, 2003).

The main exceptions to the increase in δ^{18}O with time are the very high values from the Paleoproterozoic Makganyene and Duitschland formations. These units tend to have high CIAs and are dominated by marine sedimentary clasts (carbonate and chert), suggesting that their heavy oxygen isotope compositions are influenced by incorporation of a greater proportion of preexisting sediments compared to other diamictites that contain an assortment of clast types and are often rich in igneous and meta-igneous clasts.

The increase in the average δ^{18}O values of the diamictites with time (Fig. 5a) and the increase in the range of δ^{18}O values after the Mesoarchean is broadly consistent with both the igneous δ^{18}O record provided by zircons (Valley et al., 2005) and the compilation of existing

whole-rock siliciclastic sedimentary data of Payne et al. (2015) and Bindeman et al. (2016). These studies attributed the parallel changes in the igneous and sedimentary oxygen isotope record of continents to the increased production of clay and incorporation of it into sedimentary rocks and the melting and/or magmatic assimilation of such sedimentary rocks. This increase in clay production may have been driven by a combination of crustal thickening and crustal growth, both of which led to greater amounts of emergent continental material available for weathering (Arndt, 1999; Rey and Coltice, 2008; Gaillard et al., 2011).

In summary, the above observations from major and trace elements indicate that the crust sampled by the ice sheets in the Archean was more mafic and less differentiated compared to later time periods. The similarity of these results to previous studies of Archean UCC geochemistry based on shales and map-based methods (e.g., Taylor and McLennan, 1985, 2009; Condie, 1993) strongly suggest that the diamictites are faithful proxies for the UCC composition. The presence of a negative Eu anomaly (albeit a small one) in all but one of the oldest diamictite units is consistent with Condie's (1993) contention that the average Archean UCC had a negative Eu anomaly, and its growth with time

supports the hypothesis that intracrustal differentiation increasingly became more important from late Archean onward (Taylor and McLennan, 1985). The increase in $\delta^{18}O$ values with time is also consistent (at least indirectly) with increasing recycling of continental crust from the Mesoarchean onwards, possibly the result of a thicker and more voluminous emergent crust (Payne et al., 2015).

4.3.2. Changes in the concentrations of heat producing elements

Thorium and U are two of the three major heat-producing elements in the Earth. While these elements are concentrated in the continental crust and depleted in the mantle, the amount remaining in the mantle after crust extraction plays an important role in driving convection and plate tectonics. It is for this reason, and their role as progenitors of several radiogenic Pb isotopes, that constraining the concentrations of Th and U in the upper crust is of great importance to understanding Earth differentiation and evolution.

Thorium and U are similarly incompatible during mantle melting, so the Th/U ratio in juvenile crust is expected to match the mantle ratio. While Rudnick and Gao (2003) inferred an average Th/U of 3.8 for the UCC, there are reasons to believe that the abundance of these heat-producing elements have changed through time. McLennan and Taylor (1980) and Taylor and McLennan (1985) noted a secular increase of Th/U for fine-grained sedimentary rocks, with average values between 3.5 and 4.0 for the Archean while Phanerozoic values were ~5. They attributed this trend to increased recycling of sedimentary material under oxidized atmospheric conditions after the Great Oxidation Event (GOE) around 2.4 Ga (e.g., Holland, 2006), leading to conversion of U^{+4} to soluble U^{+6} and its loss from the UCC to the oceans through weathering. Similarly, Collerson and Kamber (1999) documented a complementary decrease in the Th/U of depleted mantle through the same interval, which they attributed to increased oxidation of Earth's surface and preferential recycling of U.

The normalized concentration of Th in the diamictites shows a step-wise increase between the Mesoarchean and Paleoproterozoic (Fig. 9a), which (as mentioned above) is consistent with a more felsic and differentiated UCC after the Archean. On the other hand, the concentration of U
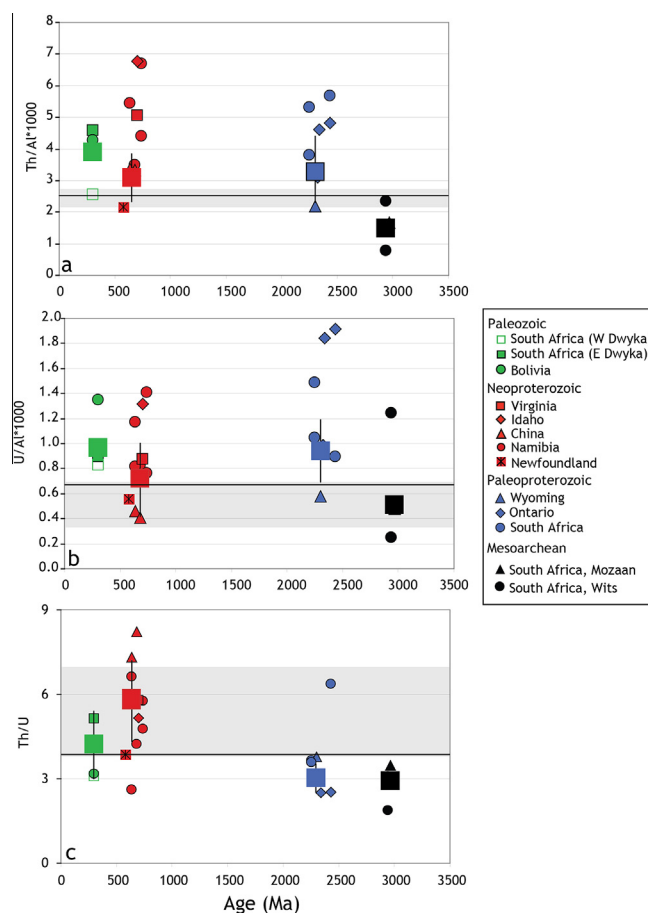

Fig. 9. Changes in Th and U with time for diamictite composites. Th and U are divided by Al (in ppm) in (a) and (b) to correct for quartz dilution effects. (a) Th shows a clear increase between the Mesoarchean and Paleoproterozoic. (b) A clear trend with age is less clear for U, but this is at least partially due to the effects of U mobility during oxidative weathering. (c) Th/U shows a steady increase with time and is highly variable in the Neoproterozoic. Both the increase and variability are likely driven by oxidative weathering, which became increasingly important after the Paleoproterozoic glaciations. UCC_RG and range of other UCC estimates are shown as a solid line and shaded area, respectively, as in Fig. 8.

shows a more subtle increase after the Archean and generally shows more scatter (Fig. 9b). The Th/U ratios of the diamictites are lower in Archean and Paleoproterozoic diamictites compared to those of the Neoproterozoic and Paleozoic (Fig. 9c), but they do not show a smooth temporal change. The Neoproterozoic samples are distinct in that they show both the greatest variation and the highest average Th/U. The temporal changes in Th/U reflect a combination of the step-wise increase in Th after the Archean and the depletion of U in most of the Neoproterozoic, Paleozoic, and one of the Paleoproterozoic (Duitschland) diamictites. The U depletion is most likely the result of oxidative weathering. Overall, the diamictite results are consistent with other UCC proxies in showing an upward redistribution of Th and U into the UCC due to enhanced intracrustal differentiation after the Archean and then loss of U to the oceans via oxidative weathering.

4.3.3. Changes in the fractionation of REEs

With the exception of Eu (discussed above), the REEs display coherent behavior during geochemical processes due to their identical oxidation states (under igneous conditions) and progressively decreasing ionic radii with increasing atomic number, which results in more incompatible behavior of the LREEs compared to the HREEs. The pressure at which partial melting and/or crystal fractionation occurs is one of the main processes controlling the fractionation of REEs, as the presence of garnet at higher pressures results in high LREE/HREE ratios in melts in equilibrium with this mineral (Drummond and Defant, 1990). Such TTGs (tonalite–trondhjemite–granodiorite associations) are a major constituent of Archean crust (e.g., Moyen and Martin, 2012). Ratios reflecting the fractionation between light, medium, and heavy REEs as a function of time are shown in Fig. 10a, c, and e. The Neoproterozoic
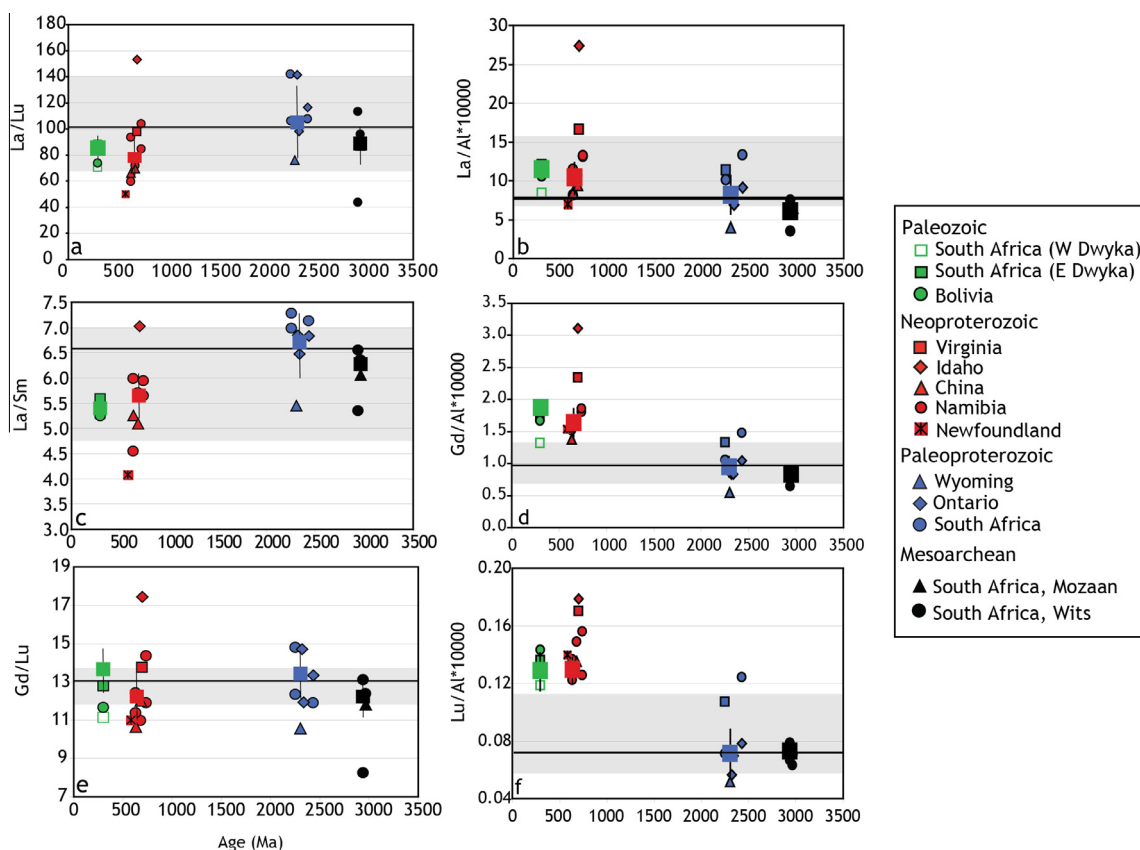

Fig. 10. Changes in REE fractionation (a, c, e) and normalized abundances (b, d, f) with time for diamictite composites. (a, c, e) La/Lu represents the fractionation between the LREE and HREEs and shows a large range for the different periods but appears to decrease slightly with time. La/Sm represents the fractionation within the LREEs and shows a significant decrease with time. Gd/Lu represents the fractionation within the HREEs and does not vary time. The changes seen in La/Lu and La/Sm may reflect a decrease in relative abundance of TTGs as a percent of the UCC and the increase in abundance of potassic "true" granites. (b, d, f) La, Gd, and Lu are given as representatives of the LREEs, MREEs, and HREEs, respectively. All elements are divided by Al (in ppm) to correct of quartz dilution effects. Increases in abundance are seen in all four elements with time and are especially marked for the MREEs and HREEs. This likely reflects both the increasingly felsic and differentiated nature of the UCC with time and the decrease in the relative proportion of TTGs to potassic granites, as the latter are more enriched in MREEs and HREEs. UCC$_{RG}$ and range of other UCC estimates are shown as a solid line and shaded area, respectively, as in Fig. 8.

Pocatello (Idaho) diamictites and one of the Mesoarchean units (the Afrikander Formation of the Witwatersrand Supergroup) are prominent outliers, which are attributable to the influence of local incompatible element-enriched rift-related igneous rocks in the case of the former (Yonkee et al., 2014) and a more mafic/ultramafic provenance of the latter (relative to the other Archean units). Even excluding these outliers, La/Lu, representing overall LREE/HREE fractionation, shows significant overlap among the four time periods (Fig. 10a). The LREEs show more resolvable differences among the four periods, with a peak in La/Sm in the Paleoproterozoic followed by a drop to lower values in the Neoproterozoic and Paleozoic (Fig. 10c). Decreasing fractionation of LREE with time is consistent with the shift from a granitic component dominated by TTG magmatism in the earlier Archean and Hadean, to "modern-style" K-rich granitic magmatism in the Neoarchean during a period of global cratonization (e.g., Whalen et al., 2004; Condie and O'Neill, 2011; Arndt, 2013; Laurent et al., 2014), a shift that is observed in a statistical analysis of the geochemistry of granites through time (Keller and Schoene, 2012). The HREEs do not show significant differences in fractionation among the four time periods, as seen in the Gd/Lu (Fig. 10e) (the latter of which is supported by a statistical test indicating data from the four time periods belong to the same population). While Archean TTGs have high Gd/Lu, they also have low concentrations of HREEs relative to Archean basalts, which tend to have flat HREE patterns (e.g., Condie, 1993). Thus, if the Gd/Lu of Archean diamictites reflects a mixture of basalt and TTG, this can explain the lack of fractionation between the Archean and post-Archean UCC.

In addition to secular changes in the fractionation of LREEs, the concentrations of the REEs (normalized to Al) change with time (Fig. 10b, d, and f). Although there is significant overlap in La concentrations in the different

time periods, Gd and especially Lu concentrations increase in younger units. This temporal increase is likely a reflection of the increasingly felsic and differentiated composition of the UCC, with the particularly marked changes in Lu (and other HREEs) likely reflecting an increasingly smaller proportion of the UCC comprised of HREE-depleted TTGs, as described above.

4.3.4. Sm/Nd and Lu/Hf

The Sm/Nd and Lu/Hf ratio are important in the study of planetary differentiation and crust formation due to their radiogenic isotopic systems (i.e., decay of ^{147}Sm to ^{143}Nd, ^{146}Sm to ^{142}Nd, and ^{176}Lu to ^{176}Hf). The Sm/Nd ratios of the diamictites show an increase between the Paleoproterozoic and Neoproterozoic (Fig. 11a), but this is an expected outcome given the change in LREE fractionation seen in Fig. 10c, and is probably attributable to the same causes. The Sm/Nd values of the diamictites are higher than in the UCC model of Rudnick and Gao (2003), and references therein; however the diamictites do not exceed the range of other published models, particularly the higher values of Kamber et al. (2005) and Chauvel et al. (2014). The diamictites show a small increase in Lu/Hf with time, but also show a much greater range for each period compared to Sm/Nd, probably due to the significantly different geochemical behavior of Lu–Hf compared to the Sm–Nd pair (Fig. 11b).

4.3.5. HFSEs

The high field strength elements (HFSE), including Zr, Hf, Nb, and Ta, are highly incompatible and enriched in the continental crust relative to the rest of the silicate Earth, but they are also insoluble in aqueous fluids and consequently are fractionated from other similarly incompatible elements (e.g., alkali and alkaline earth) during subduction zone processes (e.g., Pearce and Peate, 1995). In addition,
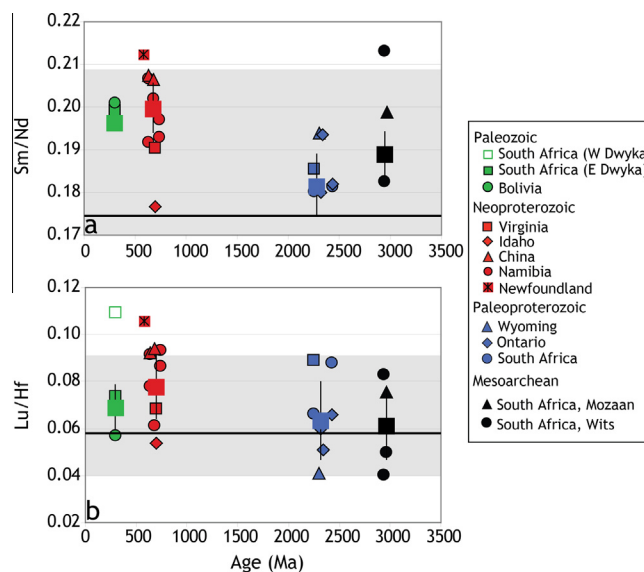

Fig. 11. (a) Sm–Nd and (b) Lu–Hf ratios in diamictite composites versus age. Significant overlap exists for all periods. Sm–Nd ratios are consistently higher than the Rudnick and Gao (2003) UCC estimate but do not exceed the full range of values in the literature. UCC_{RG} and range of other UCC estimates are shown as a solid line and shaded area, respectively, as in Fig. 8.

the pairs Zr–Hf and Nb–Ta share oxidation states and near identical ionic radii (4+, 715 pm; 5+, 640 pm, respectively) and are therefore difficult to fractionate from one another. This coherent behavior has led to their use in studies of Earth differentiation and crustal growth (e.g., Green, 1995; Barth et al., 2000; Pfander et al., 2007; Hoffmann et al., 2011).

Zr/Hf shows no secular variations, whereas Nb/Ta and La/Nb ratios of the diamictites show a jump between the Paleoproterozoic and Neoproterozoic, with older diamictites having lower Nb/Ta and higher La/Nb (Fig. 12). The latter observation is particularly interesting in light of the temporal increase in La concentrations (Fig. 10b), as it requires an even greater increase in Nb concentration in order to explain the increase in the La/Nb ratio. The lower Nb seen in the Paleoproterozoic and Mesoarchean diamictites is consistent with the other lines of evidence listed above for a greater TTG influence on the Mesoarchean and Paleoproterozoic diamictites. Although TTGs have a wide range of Nb/Ta ratios, they generally are skewed toward significantly lower ratios (e.g., Condie, 2005; Moyen and Martin, 2012). The secular changes in La/Nb and Nb/Ta ratios point to differentiation processes driving the element fractionation. The evidence from Hoffmann et al. (2011) and Marschall et al. (2013) is suggestive of a role for residual rutile in TTG genesis (McDonough, 1990; Rudnick et al., 2000).

4.4. Reexamining the integrated average UCC

The results presented here indicate that the UCC experienced a major change in composition between the Mesoarchean and Paleoproterozoic glaciations, with more subdued changes between the Paleoproterozoic and Neoproterozoic glaciations. There is no evidence from the diamictites to indicate that the UCC changed significantly in composition between the Neoproterozoic and Paleozoic, consistent with the lack of evidence for changes in crust formation and modification processes in the last billion years. Therefore, the Neoproterozoic and Paleozoic diamictites together should provide information on the average global UCC today. Below, we compare the results obtained from the Neoproterozoic and Paleozoic diamictites to previous estimates of the average UCC.

4.4.1. The major element composition of the UCC

Using the Neoproterozoic and Paleozoic diamictite samples as representative of the present-day UCC, we calculate its average major element composition. Table 4 compares UCC_{RG} to two new estimates (unfiltered and filtered) for the average UCC based on two appraisals of the Neoproterozoic and Paleozoic diamictite data. We report the median and the median absolute deviation (MAD, defined as the median of the absolute deviations of the measurements from the population median) rather than the arithmetic mean and standard deviation because the former is less influenced by outliers. Both medians are normalized to 100% anhydrous (omitting the LOI) in order to properly compare them to existing major element models. The first estimate (unfiltered) is calculated based on all Neoproterozoic and Paleozoic diamictite samples. However, a weakness of this approach is that some Namibian Neoproterozoic and the South African Paleozoic diamictites contain significant carbonate, leading to high CaO (and MgO) and unusually low values for the other major element oxides, making them clear outliers, as exemplified in Fig. 1. The second estimate (filtered) corrects for carbonate enrichment, with the median major element values providing a more robust estimate of the average UCC composition.

Major element oxide medians for the Neoproterozoic and Paleozoic are shown normalized to UCC_{RG} in Fig. 13. The filtered dataset has slightly lower MgO and CaO than the unfiltered dataset but the other major element oxides are nearly identical and all are within error of one another, indicating that carbonate-rich samples do not
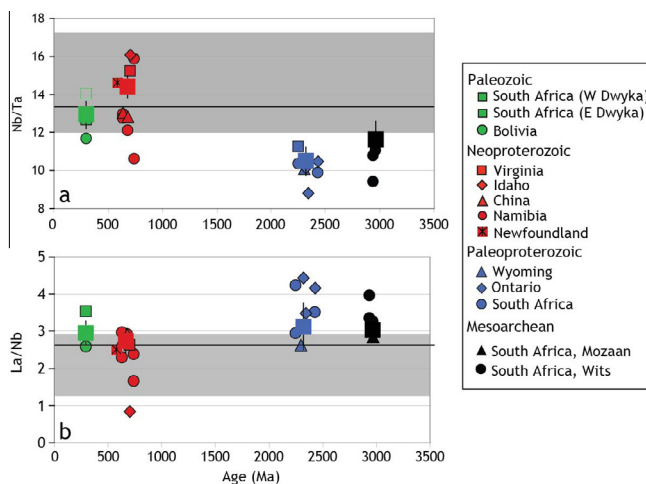

Fig. 12. HFSE ratios in diamictite composites versus age. (a) Nb/Ta shows a prominent increase between the Paleoproterozoic and Neoproterozoic, and (c) La/Nb shows an analogous decrease. This may reflect a decrease in the relative abundance of TTGs with time in the UCC. UCC_{RG} and range of other UCC estimates are shown as a solid line and shaded area, respectively, as in Fig. 8.

Table 4
Proposed model for UCC based on Neoproterozoic and Paleozoic glacial diamictites.

	Filtered to remove carbonate-rich samples		All samples		% difference (filtered vs unfiltered)	UCC$_{RG}$	%RSD[*]
	Filtered median (preferred values)	Median absolute deviation	Unfiltered median	Median absolute deviation			
(in wt%)							
SiO$_2$	70.4	2.3	70.2	2.5	0	66.2	2
TiO$_2$	0.7	0.08	0.7	0.08	0	0.63	13
Al$_2$O$_3$	14.6	0.9	14.4	1.3	1	15.3	5
Fe$_2$O$_3$(T)	5.5	0.64	5.6	1.3	−1	5.57	10
MnO	0.1	0.03	0.1	0.04	−3	0.09	13
MgO	2.0	0.35	2.2	0.42	−9	2.47	14
CaO	1.4	0.63	1.7	0.85	−17	3.57	6
Na$_2$O	1.6	0.70	1.5	0.70	7	3.25	15
K$_2$O	3.6	0.33	3.5	0.43	2	2.78	8
P$_2$O$_5$	0.2	0.03	0.2	0.03	2	0.15	15
(in ppm)							
Li	31.3	5.2	31.4	5.8	0	24.0	21
Be	2.34	0.41	2.19	0.59	7	2.08	41
Sc	12.1	1.8	12.0	2.0	1	14.0	6
V	73.8	7.2	75.0	12.1	−2	97.0	11
Cr	53.0	10.8	55.7	14.5	−5	92.3	19
Co	11.8	2.0	12.3	3.0	−4	17.3	3
Ni	26.3	5.4	27.0	7.3	−3	47.3	24
Cu	20.2	7.7	20.5	7.8	−1	27.7	14
Zn	73.0	11.4	72.0	15.0	1	67.0	9
Ga	18.2	2.1	17.6	2.5	3	17.5	4
Ge	1.66	0.14	1.61	0.21	3	1.45	9
Rb	110	20	106	21	4	82	20
Sr	91.5	30.6	99.1	30.4	−8	320	14
Y	33.2	4.5	31.0	5.0	7	21.0	11
Zr	220	31	205	39	7	193	14
Nb	12.7	1.8	12.4	2.1	2	11.8	12
Mo	0.30	0.09	0.35	0.13	−15	1.13	28
Cd	0.11	0.04	0.13	0.04	−21	0.089	15
In	0.0620	0.0136	0.0593	0.0109	4	0.0555	14
Sn	2.41	0.34	2.38	0.42	1	2.12	26
Sb	0.418	0.174	0.382	0.156	9	0.375	28
Cs	4.30	0.85	4.30	0.94	0	4.10	31
Ba	731	113	696	121	5	624	13
La	36.5	7.2	34.9	8.7	4	31.4	9
Ce	72.9	16.5	70.0	18.5	4	63.4	6
Pr	8.54	1.87	8.25	1.95	3	7.10	
Nd	33.3	6.9	31.5	6.7	6	27.0	8
Sm	6.84	1.21	6.36	1.34	7	4.70	6
Eu	1.37	0.23	1.31	0.26	4	1.02	14
Gd	6.05	1.18	5.60	1.07	8	4.01	7
Tb	0.983	0.162	0.920	0.174	7	0.650	1
Dy	5.57	0.82	5.28	0.96	5	3.91	
Ho	1.13	0.16	1.08	0.19	4	0.83	
Er	3.27	0.46	3.08	0.55	6	2.30	
Tm	0.506	0.069	0.487	0.080	4	0.300	
Yb	3.07	0.33	3.02	0.45	1	2.04	18
Lu	0.479	0.053	0.464	0.067	3	0.306	17
Hf	6.50	1.00	5.98	1.18	8	5.26	14
Ta	0.940	0.131	0.901	0.152	4	0.882	13
W	1.10	0.16	1.11	0.15	−1	1.90	54
Tl	0.588	0.187	0.544	0.179	8	0.941	57
Pb	15.8	5.1	15.1	4.9	5	17.0	3
Bi	0.24	0.08	0.22	0.09	8	0.16	38
Th	11.3	3.1	10.5	3.1	7	10.1	10
U	2.66	0.87	2.40	0.99	10	2.63	21

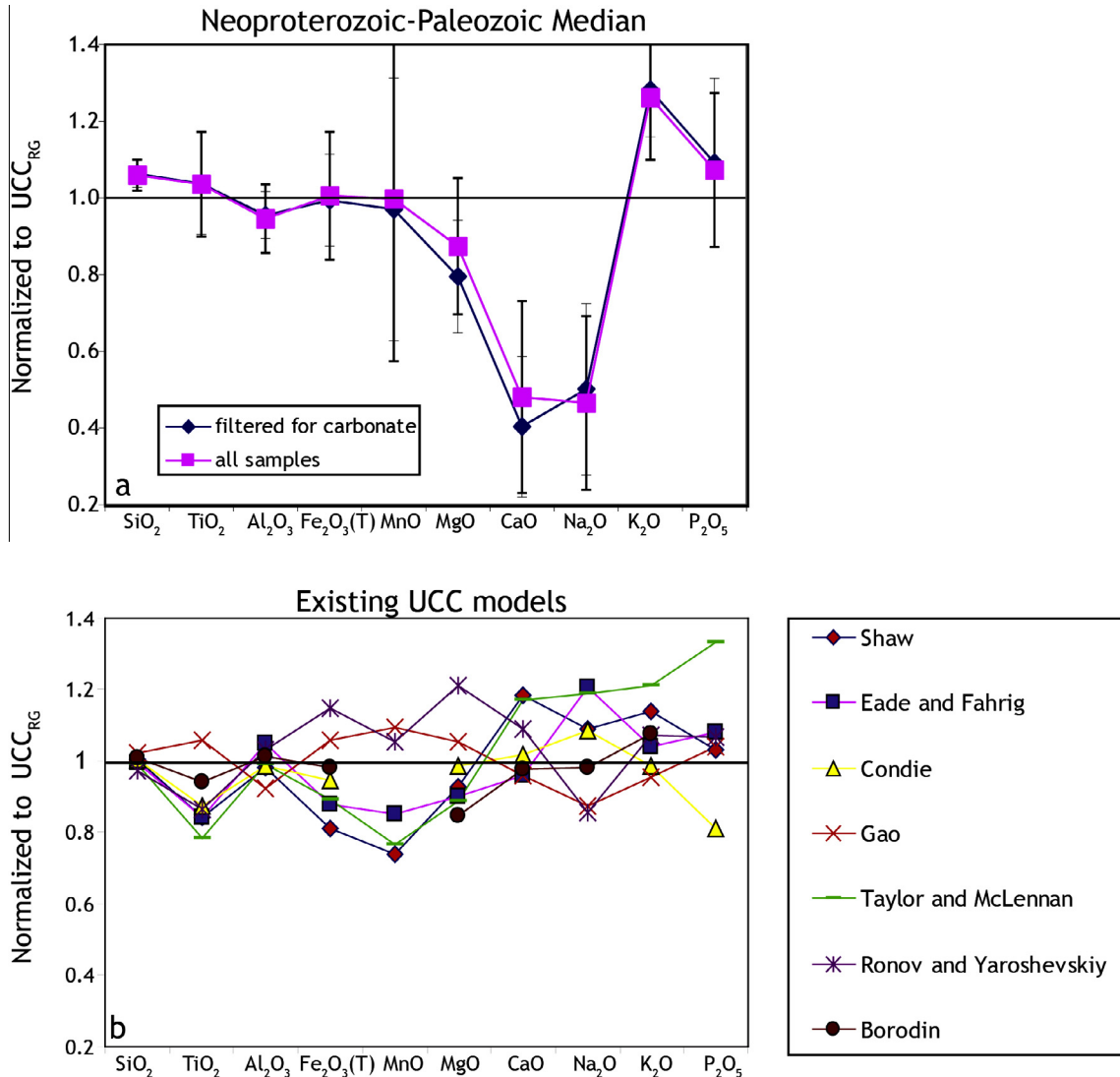[*] %RSD is based on uncertainties reported in Rudnick and Gao (2003).

Fig. 13. (a) Comparison of major elements in versions of the diamictite-based UCC model, normalized to the Rudnick and Gao (2003) UCC. The squares are derived from the median of all individual Neoproterozoic and Paleozoic samples and the diamonds are based on the median of individual samples to the right of the carbonate cut-off boundary in Fig. 1b. Error bars are median absolute deviations. (b) Major elements from other UCC models, normalized to Rudnick and Gao (2003). References: Shaw et al. (1967, 1976), Eade and Fahrig (1973), Condie (1993), Gao et al. (1998), Taylor and McLennan (1985), Ronov and Yaroshevsky (1967, 1976), and Borodin (1998).

significantly skew the results. Major differences between the Rudnick and Gao (2003) model and the diamictite-derived model are the significantly lower MgO, CaO, and Na_2O, and marginally higher K_2O of the latter. The low MgO, CaO, and Na_2O values are almost certainly the result of chemical weathering, as these major elements are highly soluble and unlikely to be fixed in secondary minerals formed during incongruent weathering (whereas K_2O can be retained if kaolinite reacts with K^+ in pore water to form illite, Fedo et al., 1995). The depletion of these elements relative to UCC_{RG} is not surprising given that this and other models cited therein are based largely on sampling crystalline bedrock of continental shields. Use of crystalline rock compositions to determine the average UCC ignores

the fact that some fraction of the UCC consists, by definition, of sediments and some fraction is chemically weathered. Accordingly, the diamictite-based model may provide a more realistic estimate of the major element composition of the UCC. However, an important question is how deeply this weathering signature extends into the crust. The thickness of UCC is typically assumed to be no more than about 10 km (e.g., Taylor and McLennan, 1985), or the approximate upper one third of the continental crust (e.g., Rudnick and Fountain, 1995). It is likely that the signature of chemical weathering that is so obvious in the diamictites attenuates with depth, but the shape of this attenuation profile is unknown and is difficult to determine.

4.4.2. The trace element composition of the UCC

A new diamictite-based estimate for the trace element composition of the UCC is presented in Table 4 based on the median values of the Neoproterozoic and Paleozoic samples. Trace element medians are shown normalized to UCC$_{RG}$ in Fig. 14. The filtered and unfiltered dataset yield median values that are within the unfiltered median absolute deviations, although the filtered dataset medians have smaller deviations. Compared to UCC$_{RG}$, the diamictite-based model yields significantly higher Li, Rb, Y, MREE, and HREE, all of which are 20–60% higher. Transitional metals Cr, Co, and Ni, along with W and Tl, are roughly 40% lower, and Sr and Mo are depleted by roughly 70% relative to UCC$_{RG}$. The depletions in Sr and Mo have already been discussed and are attributed to the effects of chemical weathering (Gaschnig et al., 2014) and the other deviations from UCC$_{RG}$ are still within the range of other UCC models (Fig. 14b). In particular, the diamictite medians for Li, Rb, Y, MREE, HREE, W, and Tl are within uncertainty of the Australian alluvium-based model of Kamber et al. (2005), and the median for Li is also similar to that of Teng et al. (2004) (35 ppm), as well as a newly proposed average UCC value based on loess analyses (Sauzéat et al., 2015) (30.5 ppm). The diamictite medians for Cr, Co, and Ni, while lower than UCC$_{RG}$, are higher than

the Shaw et al. (1967, 1976) and Eade and Fahrig (1973) models based on bedrock sampling, but are comparable to the Kamber et al. (2005) model for Cr and Ni. The diamictite median for Bi is comparable to the previous estimate of Gao et al. (1998).

4.4.2.1. Concentrations of chalcophile and siderophile elements and Be in the UCC.
Several infrequently analyzed chalcophile and siderophile elements (Ga, Ge, Cd, In, Sn, Sb, W, Tl, and Bi) were analyzed (in most cases by standard addition) in this study in order to better characterize their abundance in the UCC. We include the lithophile element Be in this discussion because it is also infrequently analyzed and its abundance in the UCC is likewise less constrained. Molybdenum was also analyzed but shows strong effects of mobilization during oxidative weathering in younger diamictites (Gaschnig et al., 2014), and consequently, it is only discussed here in the context of its relationship with Cd.

Of these elements, only Bi shows no statistical difference in concentration among the four glacial epochs. Be and Sn show the only evidence for secular changes, and both have higher concentrations in the Neoproterozoic and Paleozoic than Mesoarchean and Paleoproterozoic (red and green symbols vs. blue and black symbols, respectively, in
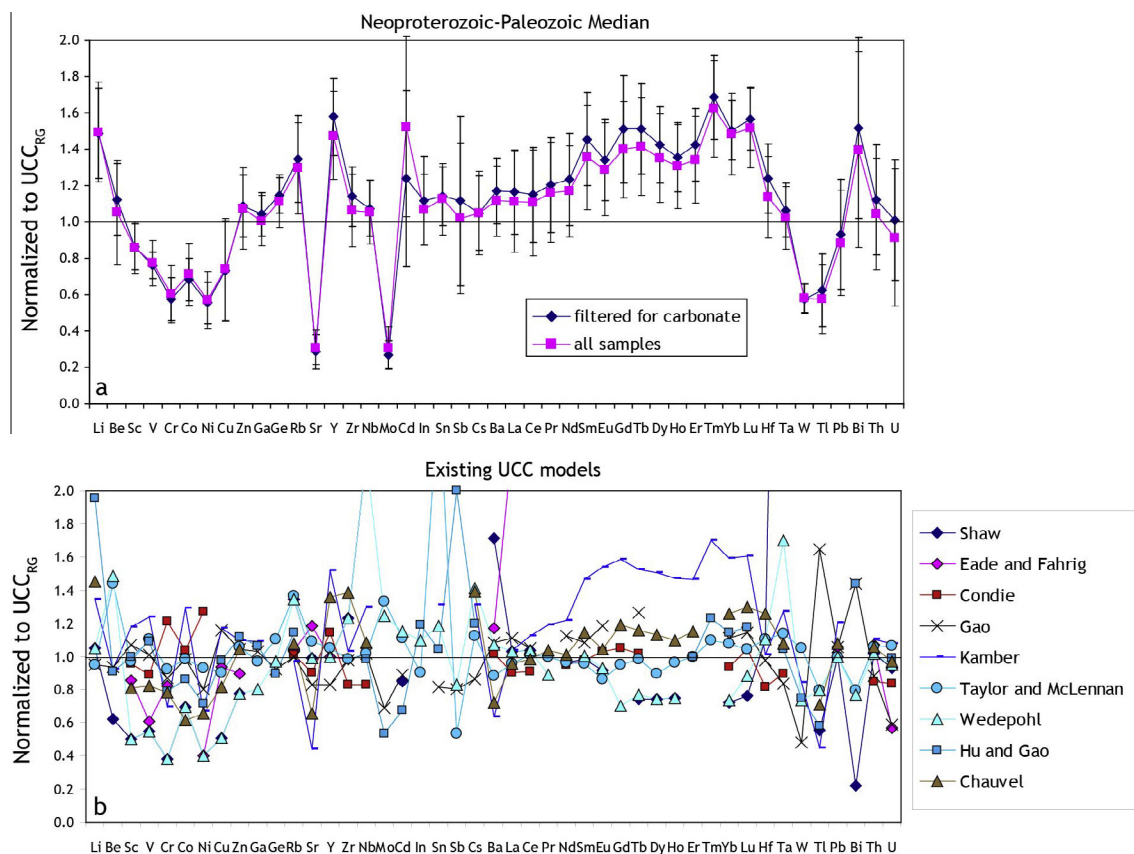

Fig. 14. Comparison of trace elements in the (a) two versions of the diamictite-based UCC model, as in Fig. 13. (b) Other UCC models are also shown. References: Shaw et al. (1967, 1976), Eade and Fahrig (1973), Condie (1993), Gao et al. (1998), Kamber et al. (2005), Taylor and McLennan (1985) including additional data from McLennan (2001), Wedepohl (1995), Hu and Gao (2008), and Chauvel et al. (2014) incorporating the Li concentration from Sauzéat et al. (2015).

Fig. 15a, b). This observation is consistent with greater differentiation of the crust through time, as both elements are incompatible and concentrated in melt during partial melting and/or fractional crystallization (e.g., Jochum et al., 1993; Ryan, 2002). Both elements correlate well with REEs, particularly Sm in the case of Be, and Yb in the case of Sn (Fig. 15a, b). Gallium correlates strongly with the other Group 13 elements, Al and In, and also with Ti, Sn, and Be (Fig. 15c). Germanium does not correlate with its Group 14 neighbors, Si and Sn, nor other trace elements, but it correlates with Fe (Fig. 15d) in older diamictite samples. Mesoarchean and Paleoproterozoic samples show correlations between Ge and Fe with differing slopes. This may indicate that Ge (which is siderophile) is following reduced iron prior to the GOE, but that this relationship does not hold for oxidized iron. Cadmium shows a complex but positive correlation with Mo (Fig. 15e) with separate diamictite units showing different Cd vs. Mo slopes. The presence or
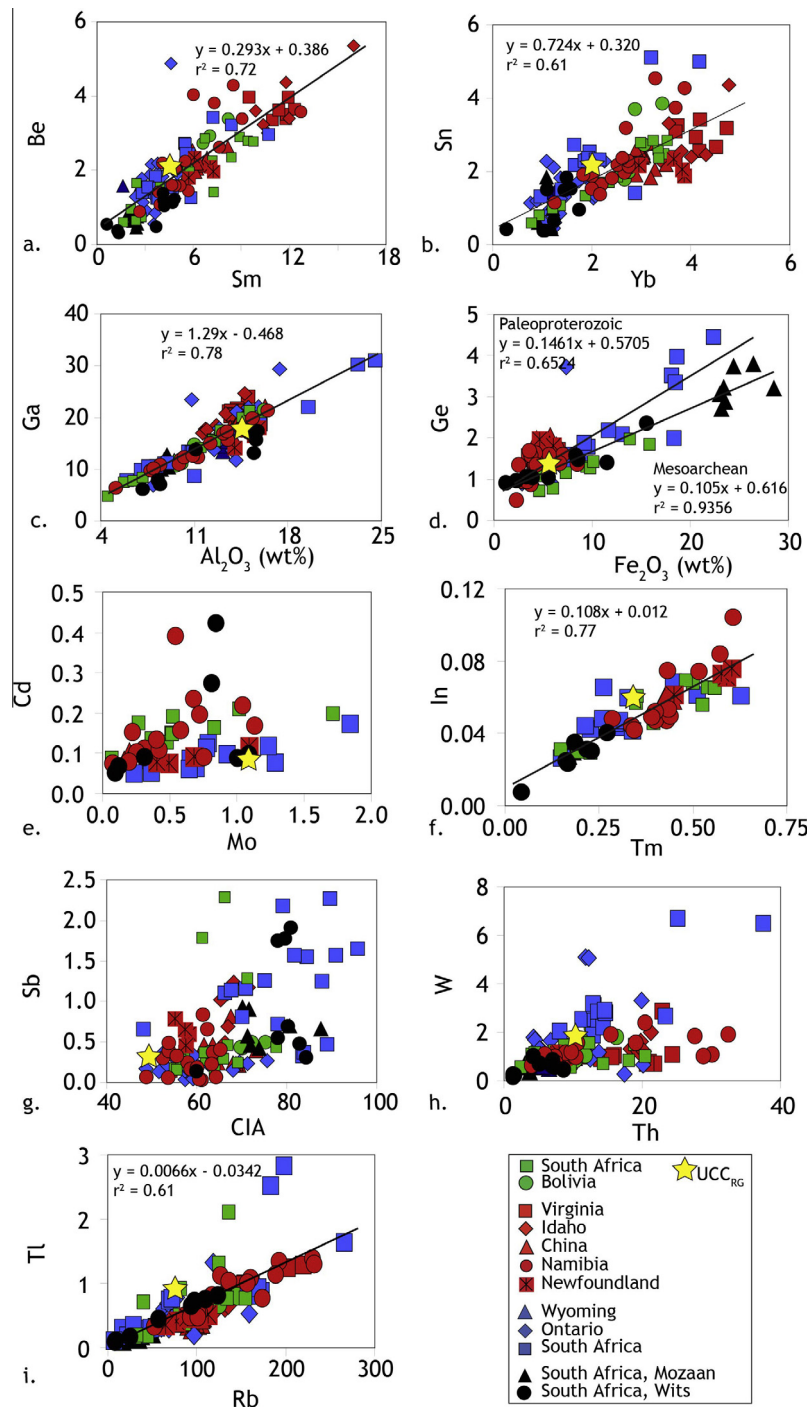
Fig. 15. Correlations seen among the chalcophile and siderophile trace elements and Be in the diamictites.

Table 5
Average upper crustal abundances of select infrequently analyzed elements derived from correlations with other elements.

	Best Est.[*]	Uncertainty (1σ)	Correlation derived[**]	Uncertainty (1σ)	Pinning element	UCC from Table 4 (diamictite median)	Uncertainty (median absolute deviation)	UCC$_{RG}$
Be	2.4	0.4	1.8	0.1	Sm	2.2	0.6	2.1
Ga	17.6	1.2	19.3	1.1	Al	17.6	2.5	17.5
In	0.066	0.009	0.044	0.003	Tm	0.059	0.011	0.055
Sn	2.54	0.30	1.74	0.27	Yb	2.38	0.42	2.12
Tl	0.69	0.13	0.52	0.12	Rb	0.54	0.18	0.94

All concentrations in ppm.
[*] Neoproterozoic/Paleozoic diamictite median for pinning element is used to calculate element of interest.
[**] Rudnick and Gao (2003) estimate for pinning element is used to calculate element of interest.

absence of oxidative weathering is the major process controlling Mo distribution in the diamictites (Gaschnig et al., 2014) and Cd may be affected by the same processes, as it is found in sulfides that are readily broken down by oxidative weathering and will remain in solution in sulfide-poor waters (e.g., Calvert and Pedersen, 1993). Indium correlates well with the MREE to HREEs and Y (Fig. 15f) and moderately well with Nb and Ta. Antimony does not correlate with other trace elements but shows a broad positive correlation with the CIA (Fig. 15g), suggesting that it may be adhering to clays during chemical weathering, although the lack of correlation with other elements with a similar tendency (e.g., Rb) suggests several processes may be at work. Tungsten correlates weakly with Th and Tl (Fig. 15g). Tl correlates well with Rb, and to a lesser extent with Th, Cs, and K (Fig. 15h). Bi does not correlate well with any other element.

Using these correlations we calculate new average UCC concentrations for chalcophile and siderophile elements. This follows the approach of McLennan (2001), where the existing average UCC concentration for a well-constrained element (the "pinning" element), along with associated uncertainties, is input into the regression equation (x in y = mx + b) to calculate a new average value for the chalcophile or siderophile element of interest. For this purpose we have used both UCC$_{RG}$ and the median values derived from the diamictites for the concentrations of the "pinning" elements. Propagating the errors on the slope and intercept of the regression, we obtain the results shown in Table 5. An obvious weakness of this general approach is that the newly-calculated concentrations are only as accurate as those for the pinning elements, and the approach can only be used in cases where correlations exist. In general, the concentrations derived from the regressions using different values for the pinning elements agree within uncertainty, and also agree with those of UCC$_{RG}$, except for Tl, with is significantly higher in the latter.

4.4.3. Toward a UCC consensus

An emerging consensus on the average abundance for many major and trace elements in the UCC can be seen in Figs. 13 and 14. All estimates of the average SiO$_2$, Al$_2$O$_3$, TiO$_2$, and K$_2$O in the UCC are within ±15%. The same is true of Ga, Ge, In, La, Ce, Nd, Pb, and Th. While much of the dispersion seen among UCC models for other

elements is attributable to chemical weathering effects, major differences are present among the insoluble first row transition metals, as well as the MREE and HREE. These differences may be the result of changing proportions of Archean to post-Archean UCC types in the sampled bedrock areas, in the case of the grid-based models, and sediment sources in the case of the sediment-based models.

5. CONCLUSIONS

Major and trace element and oxygen isotope compositions of ancient glacial diamictites from the Mesoarchean, Paleoproterozoic, Neoproterozoic, and Paleozoic paint a portrait of secular changes in the average composition of the upper continental crust with time. The diamictites indicate that the Archean UCC was dominated by greenstone belt basalt and komatiite, with subordinate TTG, and that the average UCC became more felsic and differentiated with time. These changes are consistent with previous studies that have utilized the geochemistry of shales, map-based reconstructions, and other approaches (e.g., Taylor and McLennan, 1985, 1995; Condie, 1993; Keller and Schoene, 2012), validating the utility of glacial diamictites as UCC proxies.

We use the diamictite data to develop a new model for the modern UCC composition based on the glacially sampled crust from the Neoproterozoic and Paleozoic eras. The major element trends show depletions in Ca, Na, and Mg and enrichment in K compared other UCC models, which we attribute to the effects of chemical weathering, an intrinsic characteristic of the UCC. How deep this signature extends into the crust is an important, unresolved question. The diamictite-derived trace element estimates of UCC all fall within the range of existing models, with the exceptions of large depletions in Sr and Mo that result from chemical weathering.

Of the siderophile and chalcophile elements (and Be) analyzed, only Be and Sn concentrations show evidence for secular changes in the UCC, becoming more enriched with time. Gallium behaves most similarly to Al, Ge follows Fe (for pre-Great Oxidation Event samples), Cd follows Mo, In and Sn follow the MREEs, W follows Th, and Tl follows Rb. Antimony correlates only with the CIA, and Bi does not correlate with any other element or compositional parameter. New estimates for the UCC abundances of a subset of these elements (Be, Ga, In, Sn, Tl) derived

from correlations with better-known elements and from median values for Paleozoic and Neoproterozoic diamictites are within uncertainty of UCC_{RG}, except for Tl, which is significantly higher in the latter.

APPENDIX. SUPPLEMENTARY DATA

Supplementary data associated with this article can be found, in the online version, at http://dx.doi.org/10.1016/j.gca.2016.03.020.

REFERENCES

Arndt N. (1999) Why was flood volcanism on submerged continental platforms so common in the Precambrian? *Precambr. Res.* **97**, 155–164.

Arndt N. (2013) The formation and evolution of the continental crust. *Geochem. Perspect.* **2**, 405–533.

Barth M. G., McDonough W. F. and Rudnick R. L. (2000) Tracking the budget of Nb and Ta in the continental crust. *Chem. Geol.* **165**, 197–213.

Bindeman I. N., Bekker A. and Zakharov D. O. (2016) Oxygen isotope perspective on crustal evolution on early Earth: a record of Precambrian shales with emphasis on Paleoproterozoic glaciations and Great Oxygenation Event. *Earth Planet. Sci. Lett.* **437**, 101–113.

Borodin L. S. (1998) Estimated chemical composition and petrochemical evolution of the upper continental crust. *Geochem. Int.* **37**, 723–734.

Calvert S. E. and Pedersen T. F. (1993) Geochemistry of recent oxic and anoxic marine sediments: implications for the geological record. *Mar. Geol.* **113**, 67–88.

Canil D. and Lacourse T. (2011) An estimate for the bulk composition of juvenile upper continental crust derived from glacial till in the North American Cordillera. *Chem. Geol.* **284**, 229–239.

Carto S. L. and Eyles N. (2011) The deep-marine glaciogenic Gaskiers formation, Newfoundland, Canada. In *The Geological Record of Neoproterozoic Glaciations* (eds. E. Arnaud, G. P. Halverson and G. Shields-Zhou). The Geological Society, London, pp. 467–473.

Chauvel C., Garcon M., Bureau S., Besnault A., Jahn B.-M. and Ding Z. (2014) Constraints from loess on the Hf–Nd isotopic composition of the upper continental crust. *Earth Planet. Sci. Lett.* **388**, 48–58.

Clark P. U. (1987) Subglacial sediment dispersal and till composition. *J. Geol.* **95**, 527–541.

Collerson K. D. and Kamber B. S. (1999) Evolution of the continents and the atmosphere inferred from Th–U–Nb systematics of the depleted mantle. *Science* **283**, 1519–1522.

Committee on Grand Research Questions in the Solid-Earth Sciences (2008) *Origin and Evolution of Earth: Research Questions for a Changing Planet*. National Research Council, ISBN 978-0-309-11717-3, p. 152.

Condie K. C. (1993) Chemical composition and evolution of the upper continental crust: contrasting results from surface samples and shales. *Chem. Geol.* **104**, 1–37.

Condie K. C. (2005) TTGs and adakites: are they both slab melts? *Lithos* **80**, 33–44.

Condie K. C. and Kroner A. (2013) The building blocks of continental crust: Evidence for a major change in the tectonic setting of continental growth at the end of the Archean. *Gondwana Res.* **23**, 394–402.

Condie K. C. and O'Neill C. (2011) The Archean-Proterozoic boundary: 500 my of tectonic transition in Earth history. *Am. J. Sci.* **310**, 775–790.

Cox R. N., Lowe D. R. and Cullers R. L. (1995) The influence of sediment recycling and basement composition on evolution of mudrock chemistry in the southwestern United States. *Geochim. Cosmochim. Acta* **59**, 2919–2940.

Drummond M. S. and Defant M. J. (1990) A model for trondhjemite–tonalite–dacite genesis and crustal growth via slab melting: archean to modern comparisons. *J. Geophys. Res.* **95**, 21503–21521.

Eade K. E. and Fahrig W. F. (1973) Regional, lithological, and temporal variation in the abundances of some trace elements in the Canadian Shield. *Geological Survey of Canada Paper* **72**.

Eiler J. M. (2001) Oxygen isotope variations of basaltic lavas and upper mantle rocks. *Rev. Mineral. Geochem.* **43**, 319–364.

Farmer G. L., Licht K., Swope R. J. and Andrews J. (2006) Isotopic constraints on the provenance of fine-grained sediment in LGM tills from the Ross Embayment, Antarctica. *Earth Planet. Sci. Lett.* **249**, 90–107.

Fedo C. M., Wayne Nesbitt H. and Young G. M. (1995) Unraveling the effects of potassium metasomatism in sedimentary rocks and paleosols, with implications for paleoweathering conditions and provenance. *Geology* **23**, 921–924.

Frimmel H. E. (2011) The Kaigas and Numees formations, Port Nolloth Group, in South Africa and Namibia. In *The Geological Record of Neoproterozoic Glaciations* (eds. E. Arnaud, G. P. Halverson and G. Shields-Zhou). The Geological Society, London, pp. 223–231.

Gaillard F., Scaillet B. and Arndt N. T. (2011) Atmospheric oxygenation caused by a change in volcanic degassing pressure. *Nature* **478**, 229–232.

Gallet S., Jahn B.-M., Van Vliet Lanoë B., Dia A. and Rossello E. (1998) Loess geochemistry and its implications for particle origin and composition of the upper continental crust. *Earth Planet. Sci. Lett.* **156**, 157–172.

Gao S., Luo T.-C., Zhang B.-R., Zhang H.-F., Han Y.-W., Zhao Z.-D. and Hu Y.-K. (1998) Chemical composition of the continental crust as revealed by studies in East China. *Geochim. Cosmochim. Acta* **62**, 1959–1975.

Gaschnig R. M., Rudnick R. L. and McDonough W. F. (2015a) Determination of Ga, Ge, Mo, Ag, Cd, In, Sn, Sb, W, Tl, and Bi in USGS whole-rock reference materials by standard addition ICP-MS. *Geostand. Geoanal. Res.* **39**, 371–379.

Gaschnig R. M., Rudnick R. L., McDonough W. F., Kaufman A. J., Vervoort J. D. and Fisher C. (2015b) Insights into crustal growth from detrital zircons in ancient glacial deposits: *EOS*. *EOS, Transactions, American Geophysical Union*.

Gaschnig R. M., Rudnick R. L., McDonough W. F., Kaufman A. J., Hu Z. and Gao S. (2014) Onset of oxidative weathering of continents recorded in the geochemistry of ancient glacial diamictites. *Earth Planet. Sci. Lett.* **408**, 87–99.

Goldschmidt V. M. (1933) Grundlagen der quantitativen geochemie. *Fortschritte der Mineralogie, Krystallographie und Petrographie* **17**, 112.

Goldschmidt V. M. (1958) *Geochemistry*. Oxford University Press, Oxford.

Green T. H. (1995) Significance of Nb/Ta as an indicator of geochemical processes in the crust–mantle system. *Chem. Geol.* **120**, 347–359.

Grimes C. B., Ushikubo T., John B. E. and Valley J. W. (2011) Uniformly mantle-like $\delta^{18}O$ in zircons from oceanic plagiogranites and gabbros. *Contrib. Mineral. Petrol.* **161**, 13–33.

Guy B. M., Beukes G. J. and Gutzmer J. (2010) Paleoenvironmental controls on the texture and chemical composition of pyrite from non-conglomeratic sedimentary rocks of the Mesoarchean Witwatersrand Supergroup, South Africa. *South Afr. J. Geol.* **113**, 195–228.

Hambrey, M. J. and Harland, W. B. (eds.) (1981) *Earth's Pre-Pleistocene Glacial Record*. Cambridge University Press, Cambridge.

Haskin L. A., Frey F. A., Schmitt R. A. and Smith R. H. (1966) Meteoritic, solar and terrestrial rare-earth distributions. *Phys. Chem. Earth* **7**, 167–321.

Hildes D. H. D., Clarke G. K. C., Flowers G. E. and Marshall S. J. (2004) Subglacial erosion and englacial sediment transport modelled for North American ice sheets. *Quatern. Sci. Rev.* **23**, 409–430.

Hoffman P. F. (2011) Strange bedfellows; glacial diamictite and cap carbonate from the Marinoan (635 Ma) glaciation in Namibia. *Sedimentology* **58**, 57–119.

Hoffmann J. E., Münker C., Næraa T., Rosing M. T., Herwartz D., Garbe-Schönberg D. and Svahnberg H. (2011) Mechanisms of Archean crust formation inferred from high-precision HFSE systematics in TTGs. *Geochim. Cosmochim. Acta* **75**, 4157–4178.

Hofmann M., Linnemann U., Hoffmann K.-H., Germs G., Gerdes A., Marko L., Eckelmann K., Gärtner A. and Krause R. (2015) The four Neoproterozoic glaciations of southern Namibia and their detrital zircon record: the fingerprints of four crustal growth events during two supercontinent cycles. *Precambr. Res.* **259**, 176–188.

Holland H. D. (2006) The oxygenation of the atmosphere and oceans. *Phil. Trans. Roy. Soc. Lond. B Biol. Sci.* **361**, 903–915.

Houston R. S., Karlstrom K. E., Graff P. J. and Flurkey A. J. (1992) New stratigraphic subdivisions and redefinition of subdivisions of Late Archean and Early Proterozoic metasedimentary and metavolcanic rocks of the Sierra Madre and Medicine Bow Mountains, southern Wyoming. *U.S. Geological Survey Professional Paper* **1520**.

Hu Z. and Gao S. (2008) Upper crustal abundances of trace elements: a revision and update. *Chem. Geol.* **253**, 205–221.

Jochum K. P., Hofmann A. W. and Seufert H. M. (1993) Tin in mantle-derived rocks: constraints on Earth evolution. *Geochim. Cosmochim. Acta* **57**, 3585–3595.

Kamber B. S., Greig A. and Collerson K. D. (2005) A new estimate for the composition of weathered young upper continental crust from alluvial sediments, Queensland, Australia. *Geochim. Cosmochim. Acta* **69**, 1041–1058.

Kaufman A. J., Sial A. N., Frimmel H. E. and Misi A. (2010) Neoproterozoic to Cambrian palaeoclimatic events in Southwestern Gondwana. In *Neoproterozoic-Cambrian tectonics, global change and evolution: a focus on southwestern Gondwana* (eds. C. Gaucher, A. N. Sial, G. P. Halverson and H. E. Frimmel). Elsevier, Amsterdam, pp. 369–388.

Keeley J. A., Link P. K., Fanning C. M. and Schmitz M. D. (2013) Pre- to synglacial rift-related volcanism in the Neoproterozoic (Cryogenian) Pocatello formation, SE Idaho: new SHRIMP and CA-ID-TIMS constraints. *Lithosphere* **5**, 128–150.

Keller C. B. and Schoene B. (2012) Statistical geochemistry reveals disruption in secular lithospheric evolution about 2.5 Gyr ago. *Nature* **485**, 490–493.

Klassen R. A. (1999) The application of glacial dispersal models to the interpretation of till geochemistry in Labrador, Canada. *J. Geochem. Explor.* **67**, 245–269.

Knauth L. P. and Lowe D. R. (2003) High Archean climatic temperature inferred from oxygen isotope geochemistry of cherts in the 3.5 Ga Swaziland Supergroup, South Africa. *Geol. Soc. Am. Bull.* **115**, 566–580.

Laurent O., Martin H., Moyen J. F. and Doucelance R. (2014) The diversity and evolution of late-Archean granitoids: evidence for the onset of "modern-style" plate tectonics between 3.0 and 2.5 Ga. *Lithos* **205**, 208–235.

Le Heron D. P., Busfield M. E. and Kamona F. (2013) An interglacial on snowball Earth? Dynamic ice behaviour revealed in the Chuos formation, Namibia. *Sedimentology* **60**, 411–427.

Li S., Gaschnig R. M. and Rudnick R. L. (2016) Insights into chemical weathering of the upper continental crust from the geochemistry of ancient glacial diamictites. *Geochim. Cosmochim. Acta* **176**, 96–117.

Liu C.-Q., Masuda A., Okada A., Yabuki S., Zhang J. and Fan Z.-L. (1993) A geochemical study of loess and desert sand in northern China: implications for continental crust weathering and composition. *Chem. Geol.* **106**, 359–374.

Liu X., Gao S., Diwu C. and Ling W. (2008) Precambrian crustal growth of Yangtze Craton as revealed by detrital zircon studies. *Am. J. Sci.* **308**, 421–468.

Marschall H. R., Dohmen R. and Ludwig T. (2013) Diffusion-induced fractionation of niobium and tantalum during continental crust formation. *Earth Planet. Sci. Lett.* **375**, 361–371.

Mattey D., Lowry D. and Macpherson C. (1994) Oxygen isotope composition of mantle peridotite. *Earth Planet. Sci. Lett.* **128**, 231–241.

McDonough W. F. (1990) Constraints on the composition of the continental lithospheric mantle. *Earth Planet. Sci. Lett.* **101**, 1–18.

McDonough W. F. and Sun S.-S. (1995) Composition of the Earth. *Chem. Geol.* **120**, 223–253.

McLennan S. M. (1993) Weathering and global denudation. *J. Geol.* **101**, 295–303.

McLennan S. M. (2001) Relationships between the trace element composition of sedimentary rocks and upper continental crust. *Geochem. Geophys. Geosyst.* **2**, 1021.

McLennan S. M., Fryer B. J. and Young G. M. (1979) Rare earth elements in Huronian (Lower Proterozoic) sedimentary rocks: composition and evolution of the post-Kenoran upper crust. *Geochim. Cosmochim. Acta* **43**, 375–388.

McLennan S. M., Nance W. B. and Taylor S. R. (1980) Rare earth element-thorium correlations in sedimentary rocks, and the composition of the continental crust. *Geochim. Cosmochim. Acta* **44**, 1833–1839.

McLennan S. M. and Taylor S. R. (1980) Th and U in sedimentary rocks: crustal evolution and sedimentary recycling. *Nature* **285**, 621–624.

McLennan S. M., Taylor S. R. and Kroner A. (1983) Geochemical evolution of Archean shales from South Africa. I. The Swaziland and Pongola Supergroups. *Precambr. Res.* **22**, 93–124.

Melezhik V. A., Young G. M., Eriksson P. G., Altermann W., Kump L. R. and Lepland A. (2013) Huronian-age glaciation. In *Global Events and the Fennoscandian Arctic Russia – Drilling Earth Earth Project* (eds. V. A. Melezhik, A. R. Prave, E. J. Hanski, A. E. Fallick, A. Lepland, L. R. Kump and H. Strauss). Springer-Verlag, Berlin, pp. 1059–1109.

Moyen J. and Martin H. (2012) Forty years of TTG research. *Lithos* **148**, 312–336.

Muehlenbachs K. (1998) The oxygen isotopic composition of the oceans, sediments and the seafloor. *Chem. Geol.* **145**, 263–273.

Nance W. B. and Taylor S. R. (1976) Rare earth element patterns and crustal evolution – I. Australian post-Archean sedimentary rocks. *Geochim. Cosmochim. Acta* **40**, 1539–1551.

Nance W. B. and Taylor S. R. (1977) Rare earth element patterns and crustal evolution – II. Archean sedimentary rocks from Kalgoorlie, Australia. *Geochim. Cosmochim. Acta* **41**, 225–231.

Nesbitt H. W. and Young G. M. (1982) Early Proterozoic climates and plate motions inferred from major element chemistry of lutites. *Nature* **299**, 715–717.

Ohta T. and Arai H. (2007) Statistical empirical index of chemical weathering in igneous rocks: a new tool for evaluating the degree of weathering. *Chem. Geol.* **240**, 280–297.

Payne J. L., Hand M., Pearson N. J., Barovich K. M. and McInerney D. J. (2015) Crustal thickening and clay: controls on O isotope variation in global magmatism and siliciclastic sedimentary rocks. *Earth Planet. Sci. Lett.* **412**, 70–76.

Pearce J. A. and Peate D. W. (1995) Tectonic implications of the composition of volcanic arc magmas. *Annu. Rev. Earth Planet. Sci.* **23**, 251–285.

Peucker-Ehrenbrink B. and Jahn B.-M. (2001) Rhenium–osmium isotope systematics and platinum group element concentrations: loess and the upper continental crust. *Geochem. Geophys. Geosyst.* **2**, 2001GC000172.

Potter P. E., Maynard J. B. and Depetris P. J. (2005) *Mud and Mudstones: Introduction and Overview*. Springer-Verlag, Heidelberg, p. 297.

Pfander J. A., Munker C., Stracke A. and Mezger K. (2007) Nb/Ta and Zr/Hf in ocean island basalts – Implications for crust–mantle differentiation and the fate of Niobium. *Earth Planet. Sci. Lett.* **254**, 158–172.

Prave A. R., Hoffmann K. H., Hegenberger W. and Fallick A. E. (2011) The Witvlei Group of east-central Namibia. In *The Geological Record of Neoproterozoic Glaciations* (eds. E. Arnaud, G. P. Halverson and G. Shields-Zhou). The Geological Society, London, pp. 211–216.

Rankin D. W. (1993) The volcanogenic Mount Rogers Formation and the overlying glaciogenic Konnarock Formation; two late Proterozoic units in southwestern Virginia. *U.S. Geol. Surv. Bull.* **2029**.

Rey P. F. and Coltice N. (2008) Neoarchean lithospheric strengthening and the coupling of Earth's geochemical reservoirs. *Geology* **36**, 635–638.

Ronov A. B. and Yaroshevsky A. A. (1967) Chemical structure of the Earth's crust. *Geokhimiya* **11**, 1285–1309.

Ronov A. B. and Yaroshevsky A. A. (1976) A new model for the chemical structure of the Earth's crust. *Geokhimiya* **12**, 1761–1795.

Rudnick R. (1995) Making continental crust. *Nature* **378**, 571–578.

Rudnick R. L. and Fountain D. M. (1995) Nature and composition of the continental crust: a lower crustal perspective. *Rev. Geophys.* **33**, 267–309.

Rudnick R. L., Barth M., Horn I. and McDonough W. F. (2000) Rutile-bearing refractory eclogites: missing link between continents and depleted mantle. *Science* **287**, 278–281.

Rudnick R. L. and Gao S. (2003) The composition of the continental crust. In *The Crust* (ed. R. L. Rudnick). Elsevier-Pergamon, Oxford, pp. 1–64.

Ryan J. G. (2002) Trace-element systematics of beryllium in terrestrial materials. *Rev. Mineral. Geochem.* **50**, 121–146.

Sauzéat L., Rudnick R. L., Chauvel C., Garçon M. and Tang M. (2015) New perspectives on the Li isotopic composition of the upper continental crust and its weathering signature. *Earth Planet. Sci. Lett.* **428**, 181–192.

Shaw D. M., Dostal J. and Keays R. R. (1976) Additional estimates of continental surface Precambrian shield composition in Canada. *Geochim. Cosmochim. Acta* **40**, 73–83.

Shaw D. M., Reilly G. A., Muysson J. R., Pattenden G. E. and Campbell F. E. (1967) An estimate of the chemical composition of the Canadian Precambrian Shield. *Can. J. Earth Sci.* **4**, 829–853.

Spicuzza M. J., Valley J. W. and McConnell V. S. (1998) Oxygen isotope analysis of whole rock via laser fluorination: an air-lock approach. *Abstracts with Programs – Geological Society of America* **30**, 80.

Starck D. and Papa C. d. (2006) The northwestern Argentina Tarija Basin: stratigraphy, depositional systems, and controlling factors in a glaciated basin. *J. S. Am. Earth Sci.* **22**, 169–184.

Tang M., Chen K. and Rudnick R. L. (2016) Archean upper crust transition from mafic to felsic marks the onset of plate tectonics. *Science* **351**, 372–375.

Tang M., Rudnick R. L., McDonough W. F., Gaschnig R. M. and Huang Y. (2015) Europium anomalies constrain the mass of recycled lower continental crust. *Geology* **43**, 703–706.

Taylor S. R. and McLennan S. M. (1985) *The Continental Crust: It's Composition and Evolution*. Blackwell Scientific, Oxford, p. 312.

Taylor S. R. and McLennan S. M. (1995) The geochemical evolution of the continental crust. *Rev. Geophys.* **33**, 241–265.

Taylor S. R. and McLennan S. (2009) *Planetary crusts: their composition, origin and evolution*. Cambridge University Press.

Taylor S. R., McLennan S. M. and McCulloch M. T. (1983) Geochemistry of loess, continental crustal composition and crustal model ages. *Geochim. Cosmochim. Acta* **47**, 1897–1905.

Teng F. Z., McDonough W. F., Rudnick R. L., Dalpé C., Tomascak P. B., Chappell B. W. and Gao S. (2004) Lithium isotopic composition and concentration of the upper continental crust. *Geochim. Cosmochim. Acta* **68**, 4167–4178.

Togashi S., Imai N., Okuyama-Kusunose Y., Tanaka T., Okai T., Koma T. and Murata Y. (2000) Young upper crustal chemical composition of the orogenic Japan Arc. *Geochem. Geophys. Geosyst.* **1**, 1049.

Valley J. W., Kitchen N., Kohn M. J., Niendorf C. R. and Spicuzza M. J. (1995) UWG-2, a garnet standard for oxygen isotope ratios: strategies for high precision and accuracy with laser heating. *Geochim. Cosmochim. Acta* **59**, 5223–5231.

Valley J. W., Kinny P. D., Schulze D. J. and Spicuzza M. J. (1998) Zircon Megacrysts from Kimberlite: oxygen isotope heterogeneity among mantle melts. *Contrib. Miner. Petrol.* **133**, 1–11.

Valley J. W., Lackey J. S., Cavosie A. J., Clechenko C. C., Spicuzza M. J., Basei M. A. S., Bindeman I. N., Ferreira V. P., Sial A. N., King E. M., Peck W. H., Sinha A. K. and Wei C. S. (2005) 4.4 billion years of crustal maturation: oxygen isotope ratios of magmatic zircon. *Contrib. Miner. Petrol.* **150**, 561–580.

Visser J. N. J. (1982) Upper Carboniferous glacial sedimentation in the Karoo Basin near Prieska, South Africa. *Palaeogeogr. Palaeoclimatol. Palaeoecol.* **38**, 63–92.

Vorster C. (2013) *Laser ablation ICP-MS age determination of detrital zircon populations in the Phanerozoic Cape and lower Karoo Supergroup (South Africa) and correlatives in Argentina. Ph.D. thesis* Ph. D. thesis. University of Johannesburg.

Wedepohl K. H. (1995) The composition of the continental crust. *Geochim. Cosmochim. Acta* **59**, 1217–1232.

Whalen J. B., Percival J. A., McNicoll V. J. and Longstaffe F. J. (2004) Geochemical and isotopic (Nd–O) evidence bearing on the origin of late- to post-orogenic high-K granitoid rocks in the Western Superior Province: implications for late Archean tectonomagmatic processes. *Precambr. Res.* **132**, 303–326.

Wronkiewicz D. J. and Condie K. C. (1987) Geochemistry of Archean shales from the Witwatersrand Supergroup, South Africa: source-area weathering and provenance. *Geochim. Cosmochim. Acta* **51**, 2401–2416.

Wronkiewicz D. J. and Condie K. C. (1989) Geochemistry and provenance of sediments from the Pongola Supergroup, South Africa: evidence for a 3.0-Ga-old continental craton. *Geochim. Cosmochim. Acta* **53**, 1537–1549.

Wronkiewicz D. J. and Condie K. C. (1990) Geochemistry and mineralogy of sediments from the Ventersdorp and Transvaal Supergroups, South Africa: cratonic evolution during the early Proterozoic. *Geochim. Cosmochim. Acta* **54**, 343–354.

Yonkee W. A., Dehler C. D., Link P. K., Balgord E. A., Keeley J. A., Hayes D. S., Wells M. L., Fanning C. M. and Johnston S. M. (2014) Tectono-stratigraphic framework of Neoproterozoic to Cambrian strata, west-central U.S.: Protracted rifting, glaciation, and evolution of the North American Cordilleran margin. *Earth Sci. Rev.* **136**, 59–95.

Young G. M., Minter W. E. L. and Theron J. N. (2004) Geochemistry and palaeogeography of upper Ordovician glaciogenic sedimentary rocks in the Table Mountain Group, South Africa. *Palaeogeogr. Palaeoclimatol. Palaeoecol.* **214**, 323–345.

Young G. M., von Brunn V., Gold D. J. C. and Minter W. E. L. (1998) Earth's oldest reported glaciation: physical and chemical evidence from the Archean Mozaan Group (∼2.9 Ga) of South Africa. *J. Geol.* **106**, 523–538.

Zhang W., Hu Z., Liu Y., Chen H., Gao S. and Gaschnig R. M. (2012a) Total rock dissolution using ammonium bifluoride (NH_4HF_2) in screw-top teflon vials: a new development in open-vessel digestion. *Anal. Chem.* **84**, 10686–10693.

Zhang W., Hu Z., Liu Y., Chen L., Chen H., Li M., Zhao L., Hu S. and Gao S. (2012b) Reassessment of HF/HNO_3 decomposition capability in the high-pressure digestion of felsic rocks for multi-element determination by ICP-MS. *Geostand. Geoanal. Res.* **36**, 271–289.

Zhou C., Tucker R., Xiao S., Peng Z., Yuan X. and Chen Z. (2004) New constraints on the ages of Neoproterozoic glaciations in south China. *Geology* **32**, 437–440.

Associate editor: Brian W. Stewart